Lithos 396–397 (2021) 106191

Contents lists available at ScienceDirect

Lithos

journal homepage: www.elsevier.com/locate/lithos

Synthesis Paper

Architecture of volcanic plumbing systems inferred from thermobarometry: A case study from the Miocene Gutâi Volcanic Zone in the Eastern Carpathians, Romania

Marinel Kovacs [a,*], Alexandrina Fülöp [a,1], Ioan Seghedi [b], Zoltán Pécskay [c]

[a] Tech. Univ. Cluj-Napoca, North Univ. Centre Baia Mare, Baia Mare, Romania
[b] Institute of Geodynamics Sabba S. Ştefănescu, Romanian Academy, Bucharest, Romania
[c] Institute of Nuclear Research of the Hungarian Academy of Sciences, Debrecen, Hungary

ARTICLE INFO

Article history:
Received 24 January 2021
Received in revised form 21 April 2021
Accepted 23 April 2021
Available online 28 April 2021

Keywords:
Volcanic plumbing systems
Geothermobarometry
Deep hot zone
Miocene volcanism
Eastern Carpathians

ABSTRACT

The Gutâi Volcanic Zone (GVZ) in the Eastern Carpathians records one of the most complex and long-lasting periods of Miocene volcanic activity (15.4–7.0 Ma) in the Carpathian–Pannonian region. Two types of volcanism are documented: 1) caldera-related acidic volcanism (ca. 15.4 Ma); and 2) multiphase intermediate volcanism (13.4–7.0 Ma). Two composite volcanoes (Mogoşa - G_5, Igniş - G_7), six extrusive domes (Dăneşti - G_2, Poiana Cremenei - G_3, Breze - G_6, Pleşca Mare - G_9, Gutâi - G_{10} and Laleaua Albă - G_{11}) and an intrusive complex (Firiza - G_{12}) were selected for analysis to unravel the architecture of the volcanic plumbing systems (VPS) based on the pressure-temperature (P-T) conditions during crystallisation of amphiboles and clinopyroxenes. Using the reliable geothermobarometers for amphiboles, and for clinopyroxenes, P–T conditions were calculated for basalts, basaltic andesites, andesites, dacites/rhyolites, and mafic microgranular enclaves (MMEs) hosted by dacites. The calculated pressures vary from 0.4 to 1.8 kbar for low-Al amphiboles (7.5–9.3 wt% Al_2O_3, magnesio-ferri-hornblende) and from 6 to 9 kbar for high-Al amphiboles (11.2–15.6 wt% Al_2O_3, magnesio-hastingsite, ferri-sadanagaite and pargasite). The calculated temperatures vary between 800 and 860 °C for low-Al amphiboles and between 950 and 1010 °C for high-Al amphiboles. The P–T data acquired for the clinopyroxenes (augite and diopside with 62–85 Mg#) are 3.5–8.5 kbar (predominantly >5 kbar) and 1050–1150 °C. A difference of 4–5 kbar is observed between the pressures recorded by low-Al amphiboles and clinopyroxenes in the G_2 dacites and G_3, G_6 and G_{10} high-silica andesites. The "at equilibrium" high-Al amphiboles and clinopyroxenes from the G_5, G_{11} and G_{12} samples record similar high pressures (6.0–8.5 kbar) but differences in temperature of 90–140 °C. The different depths constrained by the P–T data for the crystallisation of the amphiboles and clinopyroxenes indicate the presence of magma storage reservoirs scattered throughout the entire thickness of crust, from very deep locations (27–33 km) near the lower crust–lithospheric mantle boundary (MOHO = 33–35 km), up to shallow levels in the upper crust (2–5 km). Most of the volcanic structures show complex, multi-level interconnected VPS. The presence of numerous very deep magmatic reservoirs in several volcanic structures across the entire time-interval of the volcanism (which have high isotopic signatures, such as $^{87}Sr/^{86}Sr$ values of 0.7070–0.7076, for even the most basic rocks) provides evidence for a main, deep magma reservoir ("deep hot zone") that acted as a "MASH zone" at the crust–mantle boundary beneath the GVZ. The architecture of the magmatic plumbing systems controlled the geological evolution of the studied volcanic structures. The processes of assimilation fractional crystallisation and magma mingling and mixing were also controlled by the complex VPS, as recorded by a wide range of volcanological, mineralogical–petrographical, and geochemical features. Overall, the GVZ records a complex evolution of volcanic activity that reflects the intricate magmatic plumbing systems. The VPS models and their inferred architectures provide a better understanding of the complex and long-lasting volcanism in the GVZ, and are relevant to other areas of extinct volcanism globally.

1. Introduction

Understanding volcanic plumbing systems (VPS) is important for monitoring active volcanoes (Budd, 2015; Dahren et al., 2011). Envisaging the architecture of volcanic plumbing systems leads to a better understanding of magmatic processes that are the precursors of volcanic

* Corresponding author.
E-mail address: marinel.kovacs@cunbm.utcluj.ro (M. Kovacs).
[1] Present address: De Beers Canada-Exploration, Toronto, Ontario, Canada

https://doi.org/10.1016/j.lithos.2021.106191
0024-4937/

activity. In areas with active volcanism, geophysical data can contribute to an understanding of the depth and even the magnitude of magma reservoirs under a particular volcano. The extinct Miocene volcanism of the Gutâi Volcanic Zone (GVZ) in the Eastern Carpathians requires reconstruction of the VPS using a complex of methods such as mineralogical–petrographical, geochemical, isotopic, and geochronological analyses. Numerous investigations have focused on elucidating the structure of the VPS of many volcanoes, especially in magmatic arcs, based on the study of amphiboles and clinopyroxenes, which can reveal their conditions of crystallisation (Chadwick et al., 2013; Laeger et al., 2013; Shane and Smith, 2013; Erdmann et al., 2014; Kiss et al., 2014; Andújar et al., 2015, 2016; Cooper et al., 2016; Klaver et al., 2017; Peters et al., 2017; Sato et al., 2017; Camejo-Harry et al., 2018; Humphreys et al., 2018, 2019; Ishibashi et al., 2018; Buriánek and Kropáč, 2019; Wanke et al., 2019; Lucci et al., 2020). Various intensive parameters of crystallisation, especially P–T conditions, have been obtained by using different empirical thermobarometers and experimental studies. Most of the thermobarometers were developed on the basis of amphibole composition studies (Anderson and Smith, 1995; Blundy and Holland, 1990; Hammarstrom and Zen, 1986; Holland and Blundy, 1994; Hollister et al., 1987; Johnson and Rutherford, 1989; Krawczynski et al., 2012; Molina et al., 2015; Mutch et al., 2016; Putirka, 2016; Ridolfi et al., 2010; Ridolfi and Renzulli, 2012; Schmidt, 1992). Numerous experiments also included amphiboles to determine not only the P–T conditions, but also the compositions of the melts from which they had crystallised (Sisson and Grove, 1993; Scaillet and Evans, 1999; Pichavant et al., 2002; Grove et al., 2003; Prouteau and Scaillet, 2003; Rutherford and Devine, 2003; Barclay and Carmichael, 2004; Costa et al., 2004; Sato et al., 2005; Pietranik et al., 2009; Nandedkar et al., 2016; Blatter et al., 2017; Ulmer et al., 2018). Thermobarometers based on pyroxene compositions have also been used in many studies (Brey and Kohler, 1990; Davis and Boyd, 1966; Lindsley, 1983; Lindsley and Anderson, 1983; Wells, 1977; Wood and Banno, 1973), and especially with clinopyroxenes (Nimis, 1995, 1999; Putirka et al., 1996; Putirka, 1999; Nimis and Taylor, 2000; Putirka et al., 2003; Putirka, 2008; Neave and Putirka, 2017).

Unravelling the architecture of a volcanic plumbing system based on data from geothermobarometry has been successfully accomplished almost exclusively for individual active volcanoes using mostly pyroxene-based thermobarometers (e.g., Jeffery et al., 2013 for Kelut, Preece et al., 2014 for Merapi, Geiger et al., 2016 for Mt. Cameroon, Martel et al., 2018 for Cotopaxi, and Lucci et al., 2020 for Los Humerros). Amphibole-based thermobarometers have been underused due to the lower frequency of these minerals in the studied volcanic rocks (e.g., Turner et al., 2013 and Almeev et al., 2013 for Bezymianny volcano). Even fewer similar studies have been conducted in areas of extinct volcanism (Buriánek and Kropáč, 2019; Crossingham et al., 2018; Kamac and Altunkaynak, 2019; Kiss et al., 2014). The presence of amphiboles along with pyroxenes in several volcanic structures of the GVZ enabled the use of both amphibole- and clinopyroxene-based thermobarometers for our study.

The Gutâi Volcanic Zone is one of the most complex volcanic areas in the Carpathian–Pannonian region, with long-lasting Miocene volcanism (15.4–7.0 Ma; Pécskay et al., 2006) and intricate magmatic processes such as assimilation fractional crystallisation (AFC) and magma mixing (Kovacs et al., 2017). For a better understanding of the volcanic evolution, we attempted to unravel the architecture of the VPS in several composite volcanoes, such as the extrusive lava domes and intrusive magmatic bodies emplaced between 11.6 and 7.0 Ma in the central–southern area of the GVZ. Amphiboles and clinopyroxenes were selected from the basalts, basaltic andesites, andesites, dacites and mafic microgranular enclaves (MMEs) hosted by dacite in nine volcanic structures (Appendix 1, Supplementary Data) and used to calculate the P–T parameters, based on the thermobarometer of Putirka (2016) for amphiboles, and Putirka (2008) and Neave and Putirka (2017) for clinopyroxenes. A geothermobarometric study of these volcanic rocks is key to understanding the architecture of the magma plumbing systems of the respective volcanoes. This is the first study attempting to model the VPS in the Gutâi Volcanic Zone and also the first study encompassing several volcanic structures in the Carpathian-Pannonian region.

2. Geological setting

The Maramureş area, including the GVZ, is situated in the northern part of the Carpathian–Pannonian region, which from a tectonic point of view includes two continental plates (megaunits), namely the ALCAPA (ALpine-CArpathian-PAnnonian) and Tisza–Dacia plates (e.g., Csontos et al., 1992), which are juxtaposed along a transpressional fault zone (the Mid-Hungarian Fault Zone; MHFZ, Fig. 1a; e.g., Balla, 1987 and Csontos, 1995). The study area lies in the interior of the Carpathian mountain chain in a geologically complex area, where several geological units situated at the easternmost tip of the ALCAPA Plate were thrust over the Tisza–Dacia Plate to the south (Tischler et al., 2008 and references therein). The Maramureş area and the entire region belonging to the present Transcarpathian Basin (parts of the ALCAPA Plate) broke up along numerous normal fault systems (Márton et al., 2007) prior to the amalgamation with the European foreland (e.g., Andreucci et al., 2015) during opposing rotations of the ALCAPA and Tisza–Dacia plates at ca. 18.5 Ma. During the middle–late Miocene, sedimentation and extensive volcanism (e.g., Konečný et al., 2002; Pécskay et al., 2006; Seghedi et al., 2001, 2004), considered to be post-collisional (Seghedi and Downes, 2011), began in the present Transcarpathian Basin (TB), which decoupled from the western ALCAPA Plate after 12 Ma and a final anticlockwise rotation of ~30° (Márton et al., 2007).

The E–W-striking Bogdan–Dragoş–Vodă fault system that bounds the Maramureş area to the south has accommodated several stages of extensional (18.5–16 Ma), transpressional (16–12 Ma) and transtensional (12–10 Ma) deformation (Tischler et al., 2007, 2008; Gröger et al., 2008; Fig. 1a).

Widespread volcanism within the TB produced a series of volcanic fields, namely, Tokaj, Zemplín, Slanské vrchy, Vihorlat, Gutin, Beregovo and Oaş–Gutâi (e.g., Lexa et al., 2010) (Fig. 1a). Volcanic activity peaked between ca. 14 and 9 Ma in terrestrial and shallow-marine environments (Pécskay et al., 2006).

Three types of magmatic activity are recognised in the Transcarpathian Basin: (1) acidic volcanism that is constrained to a caldera source (Fülöp, 2003) and similar to the acidic volcanism developed throughout the entire Carpathian–Pannonian region (Pécskay et al., 1995, 2006; Lexa et al., 2010; Lukacs et al., 2018), and which is dated at 15.4–14.4 Ma (de Leeuw et al., 2013; Szakács et al., 2012); (2) intermediate volcanism of late Badenian to early Pannonian age (14.5–9.0 Ma; Pécskay et al., 2006) in the Slanské vrchy, Vihorlat, Gutin and Gutâi mountains along the margins of the TB (Kovacs et al., 2013, 2017; Lexa et al., 2010; Seghedi et al., 2001); (3) late Badenian to early Pannonian (13.5–9.0 Ma; Pécskay et al., 2006; Szepesi et al., 2019 and references therein) bimodal intermediate–acid volcanism in the inner part of the TB (e.g., the Tokaj–Zemplín–Beregovo–Oaş volcanic areas).

Most of the existing geodynamic models explain the evolution of the Carpathian–Pannonian system by classical subduction zone processes (e.g., Horváth, 1993; Konečný et al., 2002), but this explanation has been challenged recently by models involving gravitational instability of the mantle lithosphere (e.g., Dando et al., 2011; Houseman and Gemmer, 2007). In a recently published article on the Oaş–Gutâi Volcanic Zone, a drip model has been suggested for the magmas in the Transcarpathian Basin as an alternative to the initiation of lithosphere melting (Kovacs et al., 2017).

The Gutâi Volcanic Zone (GVZ) is a segment of the Neogene–Quaternary volcanic chain of the Carpathians, which stretches over the northeastern part of Romania (Eastern Europe). Two types of volcanic activity have been documented in the Gutâi Volcanic

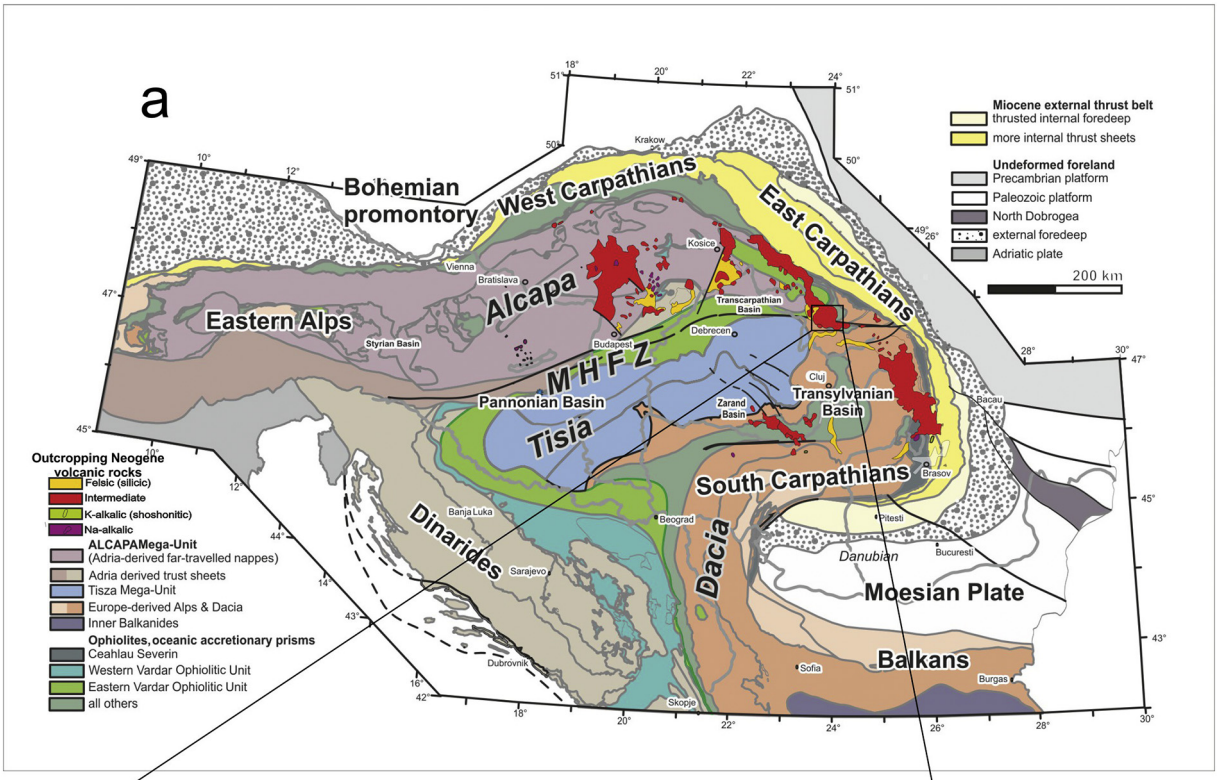
a
Miocene external thrust belt
thrusted internal foredeep
more internal thrust sheets
Undeformed foreland
Precambrian platform
Paleozoic platform
North Dobrogea
external foredeep
Adriatic plate
200 km
Bohemian promontory
West Carpathians
East Carpathians
Eastern Alps
Alcapa
Tisia
Dinarides
Dacia
Pannonian Basin
Transylvanian Basin
South Carpathians
Moesian Plate
Balkans
Danubian
M H F Z
Styrian Basin
Transcarpathian Basin
Zarand Basin
Vienna
Bratislava
Budapest
Debrecen
Kosice
Krakow
Cluj
Brasov
Bacau
Pitesti
Bucuresti
Beograd
Banja Luka
Sarajevo
Dubrovnik
Skopje
Sofia
Burgas
Outcropping Neogene volcanic rocks
Felsic (silicic)
Intermediate
K-alkalic (shoshonitic)
Na-alkalic
ALCAPAMega-Unit
(Adria-derived far-travelled nappes)
Adria derived trust sheets
Tisza Mega-Unit
Europe-derived Alps & Dacia
Inner Balkanides
Ophiolites, oceanic accretionary prisms
Ceahlau Severin
Western Vardar Ophiolitic Unit
Eastern Vardar Ophiolitic Unit
all others

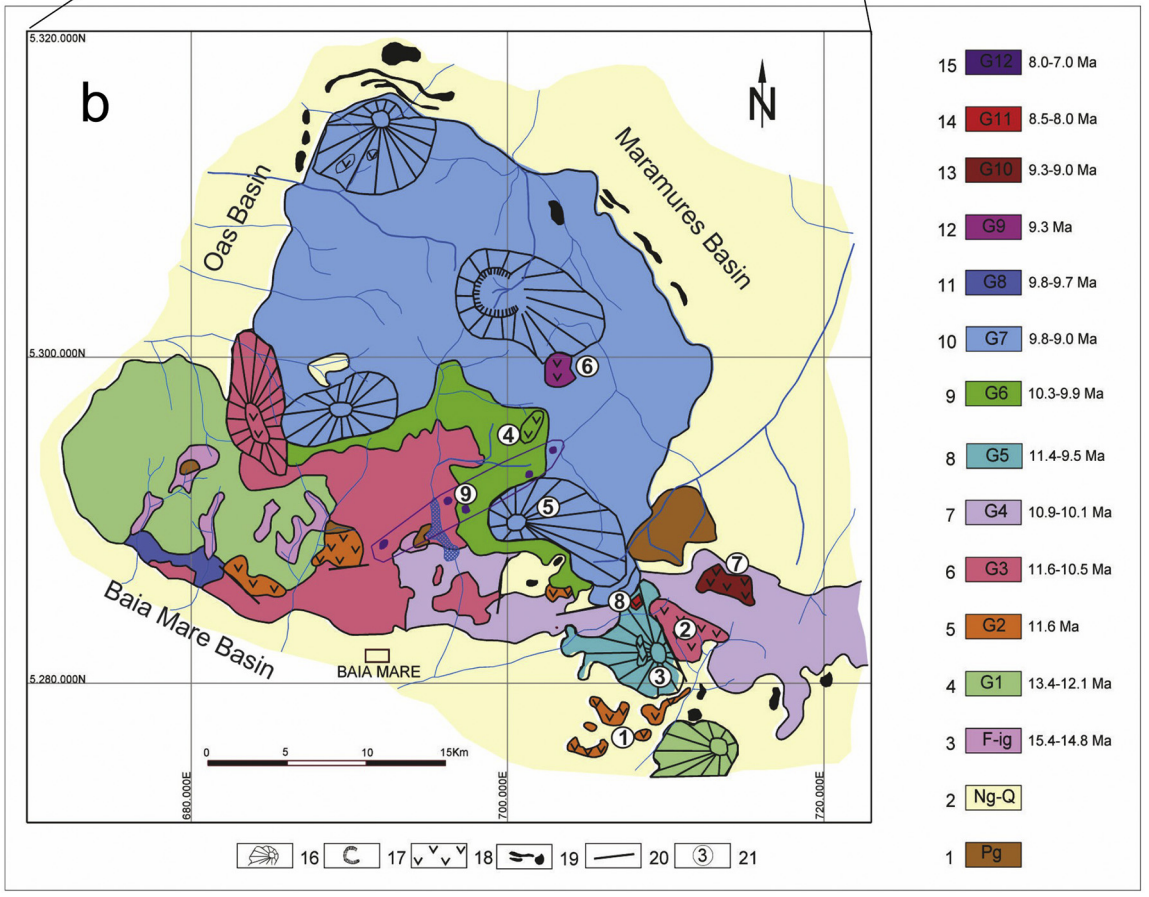
b
N
Oas Basin
Maramures Basin
Baia Mare Basin
BAIA MARE
5.320.000N
5.300.000N
5.280.000N
680.000E
700.000E
720.000E
0 5 10 15Km
15 G12 8.0-7.0 Ma
14 G11 8.5-8.0 Ma
13 G10 9.3-9.0 Ma
12 G9 9.3 Ma
11 G8 9.8-9.7 Ma
10 G7 9.8-9.0 Ma
9 G6 10.3-9.9 Ma
8 G5 11.4-9.5 Ma
7 G4 10.9-10.1 Ma
6 G3 11.6-10.5 Ma
5 G2 11.6 Ma
4 G1 13.4-12.1 Ma
3 F-ig 15.4-14.8 Ma
2 Ng-Q
1 Pg
16 17 18 19 20 21

Zone: 1) caldera-related acidic volcanism (initiated at ca. 15.4 Ma; Fülöp, 2002, 2003) that yielded a complex assemblage of ignimbrites and resedimented counterparts in the southwestern part of the volcanic area (Fig. 1b); and 2) intermediate multiphase volcanism (13.4–7.0 Ma; Kovacs and Fülöp, 2003) that generated numerous volcanic structures including composite volcanoes, extrusive domes and intrusions. The intermediate volcanism developed in four stages across the GVZ. The first two stages produced >85% of the total volcanic products piled up in multiple overlapping volcanic complexes (Kovacs et al., 2017). The volcanism reached its climax during the second stage (11.6–9 Ma), when subalkaline, predominantly medium-K basaltic andesites, andesites and dacites were generated. A total of nine volcanic structures (G_2–G_{10} described in Kovacs et al., 2017) were assigned to the second stage of the ntermediate/andesitic volcanism (Fig. 1b). A small composite dome of high-silica andesite and dacite was emplaced in the third stage (G_{11}, 8.5–8.0 Ma; Kovacs, 2002; Kovacs et al., 2017), and several dykes of clinopyroxene + olivine basalt mark the end of volcanic activity in the fourth stage (G_{12}, 8.1–7.0 Ma; Edelstein et al., 1993; Kovacs et al., 2017; Fig. 1b).

The volcanic structures selected for our geothermobarometric study were generated during the second, third and fourth stages of the intermediate volcanism (G_2, G_3, G_5, G_6, G_7, G_9 and G_{10} of stage II, and G_{11} and G_{12} of stages III and IV). Data for the studied volcanic structures are given in Table 1 and Appendix 1 of the Supplementary Data.

On the Peccerillo–Taylor diagram (Fig. 2), the rocks plot as calc-alkaline medium- to high-K, and they are the surface expression of magmatic processes dominated by AFC and magma mixing. Most of the high-silica andesites (≥60 wt% SiO_2) and dacites in extrusive lava domes are hybrid products of magma mingling and mixing (Kovacs et al., 2014; Naumov et al., 2014). In some composite domes, hybrid dacites and/or rhyolites are encountered in the core and enclosed by high-silica andesites and/or dacites in the rim (e.g., the Dăneşti composite dome (G_2) and the Pleşca Mare dome (G_9); Fig. 1b; Kovacs et al., 2014, 2017).

The magmatic processes were controlled by magmas that originated in lithospheric mantle that had been modified by subduction components, and with the evolution of the magmas taking place in intracrustal multi-level interconnected magma reservoirs (Kovacs et al., 2017).

3. Sampling and analytical methods

Six volcanic structures and one intrusive magmatic complex consisting of rocks with amphibole and clinopyroxene, and two volcanic structures with clinopyroxene but no amphibole, were selected for EPM analyses of the amphiboles and clinopyroxenes. More than 300 thin sections were examined under the optical microscope to characterise the mineralogical assemblages and textural features of the volcanic rocks, with a focus on the amphiboles and clinopyroxenes. The EPM analyses were performed at Queen's University, Kingston, Canada, using a JEOL JXA-8230 electron probe microanalyser (EPMA). An accelerating potential of 15 kV, a beam current of 20 nA and an electron beam diameter of 2 μm were applied for all analysed minerals. Kα X-ray lines were used for analyses of all elements. The standards and diffracting crystals for the analysed elements were as follows: Si, natural and synthetic diopside, TAP; Al, natural anorthite, USNM 137041, TAP; Ti, natural rutile, NMMH 120812, LPET; Cr, synthetic Cr_2O_3, LLIF; Fe, synthetic fayalite, LLIF; Mn, natural rhodonite, Harvard 104,791, LLIF; Mg, synthetic diopside and natural diopside, PSU Px-1, TAP; Ca, synthetic and natural diopside, PSU Px-1, and natural wollastonite, PET; Na, natural albite, TAP; K, natural adularia, PSU Or-1, PETH; F, synthetic fluorophlogopite, TAP; and Cl, tugtupite, ROM M32790, PETH. The matrix correction procedure was used for spectra processing, namely the PAP model of Pouchou and Pichoir (1991) for the atomic number and absorption corrections, and the Reed (1990) and Springer (1971) models for the secondary fluorescence correction.

A total of 344 analyses (150 amphiboles and 194 clinopyroxenes) were used for this geothermobarometric study, including 95 analyses performed previously at the University of Würzburg and published by Kovacs (2002).

4. Results

4.1. Amphiboles and clinopyroxenes in the investigated rocks

The amphiboles occur as euhedral or subhedral and mainly prismatic phenocrysts of different sizes, generally between 0.1 and 3.0 mm and rarely up to 10 mm in the G_2 and G_{11} dacitic rocks and G_{12} basalts (Fig. 3a). The largest, 3 cm in size, are macrocrysts in the G_5 basaltic andesites (Fig. 3b) and the gabbroic mafic enclaves hosted by the G_{11} dacites. The crystals often exhibit rims of variable thickness that consist of, or are entirely replaced by, clinopyroxene + plagioclase + Fe—Ti oxides (Fig. 4b). Amphibole represents up to 10% of all phenocrysts in the G_2 and G_{11} dacites, up to 5% in the G_3, G_6 and G_{10} high-silica andesites, and < 5% in the G_5 basaltic andesites and G_{5a} high-silica andesites/dacites. In the G_{12} basalts, the amphiboles occur sporadically. In the MMEs of the G_{11} dacites and G_{5a} high-silica andesites/dacites, the amphiboles make up to 70% of the rock.

Overall, the amphiboles are texturally and compositionally homogeneous, with no optical zoning (Fig. 4a, b). Rare normally zoned crystals occur in the high-silica andesites and dacites of G_2, G_3, G_{10} and G_{11} (Fig. 4c).

The clinopyroxenes are single euhedral to subhedral crystals, or form clusters with orthopyroxene, plagioclase and Fe—Ti oxides (Fig. 3c, d). Clinopyroxene sizes range from ≤1 mm to 1 cm. Their modal abundance may reach 20% of all phenocrysts in the G_5 and G_{12} basaltic rocks, whereas in the G_2, G_6, G_9, G_{10} and G_{11} high-silica andesites and dacites they represent <5%.

In the G_3, G_5 and G_6 volcanic rocks, the clinopyroxenes commonly display slight normal or oscillatory zoning (Fig. 4e). In the G_{11} dacites and G_{12} olivine-bearing basalts, the clustered clinopyroxenes frequently show more intense zoning (Fig. 4f). Inclusions of Ti—Fe oxides are common in all of the clinopyroxenes.

4.2. Mineral chemistry

All of the amphibole analyses used for the P–T calculations are given in Appendix 4 of the Supplementary Data. Selected analyses are presented in Table 2.

The amphibole formulae were calculated from the EPM data based on the stoichiometric considerations of Hawthorne et al. (2012) and using the software of Locock (2014, Appendix 3, Supplementary Data). All of the studied amphiboles are calcic according to IMA recommendations (Hawthorne et al., 2012; Fig. 5a). A series of amphiboles that are

Fig. 1. a. Simplified sketch map of the Carpathian–Pannonian region (after Schmid et al., 2008) showing outcropping Miocene–Quaternary magmatism (simplified after Pécskay et al., 2006); MHFZ-Mid Hungarian Fault Zone; Location of the study area in the frame. b. Simplified geological/volcanological map of the Gutâi Volcanic Zone/GVZ with the distribution of the investigated volcanic structures. Sedimentary deposits: Paleogene (1); Neogene-Quaternary (2); Miocene volcanic complexes (Kovacs et al., 2017): Felsic/rhyolitic volcanic rocks-ignimbrites (3); Intermediate/andesitic volcanic rocks: Stage one: G_1 (4); Stage two: G_2 - G_{10} (5–13); Stage three: G_{11} (14); Stage four: G_{12} (15); Composite volcano (16); Crater (17); Extrusive dome (18); Intrusion (19); Fault (20). Studied volcanic structures (21): 1: Dăneşti composite dome (G_2); 2: Poiana Cremenei extrusive dome (G_3); 3: Mogoşa composite volcano (G_5); 4: Firiza andesitic complex and Breze dome (G_6); 5: Igniş volcano (G_7); 6: Pleşca Mare composite dome (G_9); 7: Gutâi extrusive dome (G_{10}); 8: Laleaua Albă composite dome (G_{11}); 9: Firiza basaltic intrusions (G_{12}).

Table 1
The age, petrography-mineralogy and analysed minerals of the studied volcanic structures. Pl - plagioclase; San - sanidine; Ol - olivine; Px - pyroxene; Cpx - clinopyroxene; Amph - amphibole; Bi - biotite; Qtz - quartz; Ma - million years.

Volcanic structures	Age (Ma)	Rock type	Mineralogy	EMP analyses
G_{12}: Firiza intrusions (dykes)	8.1–7.0	Basalts	Pl + Px + Ol + Amph	Amph, Cpx
G_{11}: Laleaua Albă composite dome	8.5–8.0	1. High Si andesites	Pl + Px + Amph+Bi+Qtz	Amph, Cpx
		2. Dacites (with MME)	Pl + San + Bi+Qtz + Amph+Px	Amph, Cpx
G_{10}: Gutâi dome	9.3–9.0	High Si andesites	Pl + Px + Amph+Bi+Qtz	Amph, Cpx
G_9:Pleşca Mare composite dome	9.0	1. High Si andesites	Pl + Px + Bi+Qtz	Cpx
		2. Dacites	Pl + Bi+Qtz + Px	Cpx
G_7: Igniş composite volcano	9.5–9.0	High Si andesites	Pl + Px	Cpx
G_6: Breze lava flows and lava dome	10.3–9.9	High Si andesites	Pl + Px + Amph	Amph, Cpx
		Dacites	Pl + Amph+Px	Amph
G_5: Mogoşa composite volcano	11.4–9.5	1. Basaltic andesites	Pl + Px	Cpx
		2. High Si and/dacites	Pl + Px + Amph	Amph, Cpx
		3. Basaltic andesites	Pl + Px + Amph	Amph, Cpx
G_3: Poiana Cremenei dome	11.3.	High Si andesites	Pl + Px + Amph+Qtz	Amph, Cpx
G_2: Dăneşti composite dome	11.6.	1. Dacites	Pl + Px	Cpx
		2. Dacites/Rhyolites	Pl + Bi+Qtz + Amph+Px	Amph, Cpx

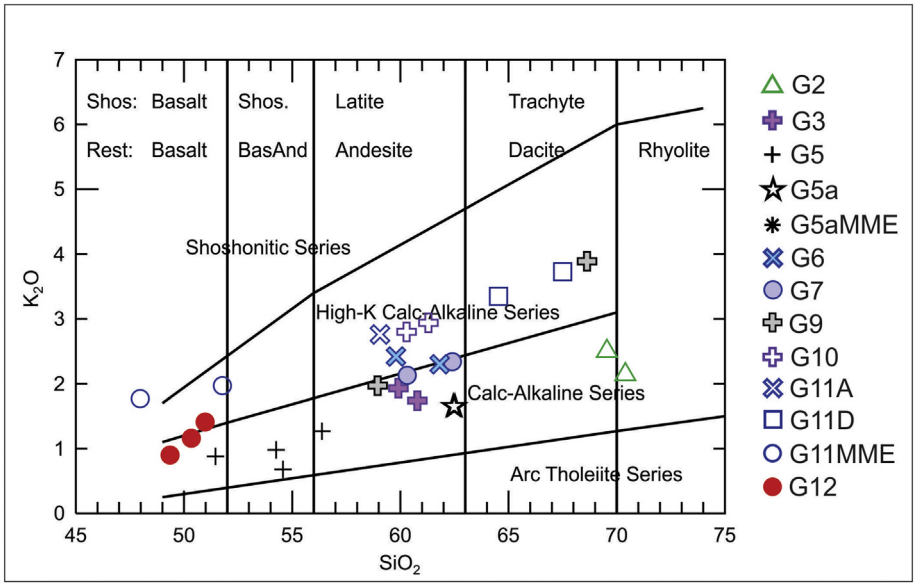

Fig. 2. Distribution of the volcanic rocks from the studied volcanic structures in Peccerillo-Taylor diagram. G_2, G_3, G_5, G_6, G_7, G_9, G_{10}, G_{11} & G_{12} are the nine volcanic structures represented in Fig. 1b; G_{5a}: Valea Morii dome from Mogoşa composite volcano; G_{5a} MME: mafic microgranular enclaves from Valea Morii dome rocks; G_{11}A: high-silica andesites from Laleaua Albă composite dome; G_{11}D: dacites from Laleaua Albă composite dome; G_{11}MME - mafic microgranular enclaves from Laleaua Albă dacites.

classified as pargasites and/or sadanagaites on Fig. 5a are reclassified as magnesio-hastingsites based on the formulae calculated using the methods of Locock (2014).

There are two types of amphibole: 1) low-Al amphiboles (7.0–9.5 wt% Al_2O_3), represented exclusively by magnesio-ferri-hornblendes, which are typical of the high-silica andesites and dacites of G_2, G_3, G_6 and G_{10}, and 2) high-Al amphiboles (11.2–15.6 wt% Al_2O_3), represented by magnesio-hastingsites, sadanagaites and pargasites, and which are typical of G_5 (basaltic andesites, high-silica andesites/dacites and MMEs), G_{11} (high-silica andesites, dacites and MMEs) and G_{12} (pyroxene + olivine basalts). There is remarkable similarity among the aluminium contents of amphiboles from the same volcanic structure, and they show insignificant internal zoning or an absence of zoning. Multiple measurements across the amphiboles from the G_2 dacite/rhyolite (Fig. 4a) and G_5 basaltic andesite yielded 7.7–8.2 and 12.2–12.8 wt% Al_2O_3, respectively. Rare crystals of magnesio-ferri-hornblende from the G_2, G_3 and G_{10} volcanic rocks exhibit higher Al cores (11.2–12.0 wt% Al_2O_3) corresponding to magnesio-hastingsite, which suggests an antecrystic origin. A single amphibole crystal from the mafic enclave hosted by the G_{11} dacite contains an unexpectedly low-Al_2O_3 rim of 9.5 wt%, compared with the >12.8 wt% Al_2O_3 of all other measured points.

SiO_2 correlates inversely with Al in these amphiboles, and SiO_2 ranges from 43.7 to 46.6 wt% in the low-Al amphiboles (magnesio-ferri-hornblendes from G_2, G_3, G_6 and G_{10}) and from 37.5 to 42.3 wt% in the high-Al amphiboles (ferri-sadanagaites, magnesio-hastingsites and pargasites from G_5, G_{11} and G_{12}). SiO_2 also correlates inversely with TiO_2 so that the Ti-rich high-Al amphiboles contain the lowest contents of SiO_2.

A good correlation between TiO_2 and Al_2O_3 characterises the analysed amphiboles, so that TiO_2 contents are 0.9–2.0 wt% in the low-Al amphiboles and 2.3–3.5 wt% in the high-Al amphiboles. A similar correlation exists between MgO and Al_2O_3, with the low-Al amphiboles having a range of 9.3–12.7 wt% MgO, and the high-Al amphiboles a range of 12.5–14.5 wt% MgO. In contrast, FeO contents are higher (15.6–21.0 wt%) in the low-Al amphiboles and lower (10.0–14.7 wt%) in the high-Al amphiboles.

The two types of amphibole show distinct Al^{IV} contents and Mg numbers (Mg#), which correlate well with their origins as phenocrysts,

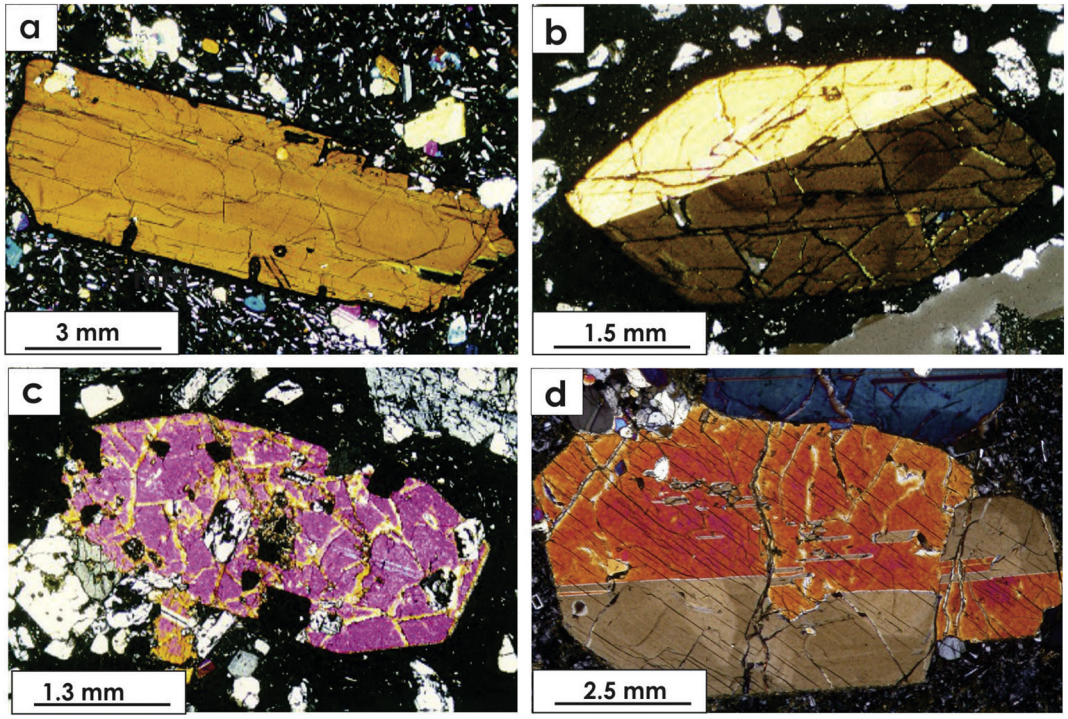

Fig. 3. Photomicrographs of the amphiboles and clinopyroxenes from the GVZ volcanic rocks. a. Ti-rich magnesio-hastingsite macrocryst from the G_{12} olivine-bearing basalts; b. Large-sized amphibole (ferri-sadanagaite) from the G_5 basaltic andesites; c. Ti-augite phenocryst from the G_5 basaltic andesites; d. Large Cr-diopside xenocryst from the G_{11} high-silica andesites.

antecrysts or xenocrysts. Thus, magnesio-ferri-hornblende phenocrysts in the G_2 dacites have Al^{IV} = 1.20–1.42 and Mg# = 50–57, whereas magnesio-hastingsite xenocrysts in the G_{11} dacites have Al^{IV} = 1.78–2.35 and Mg# = 72–81. In the MMEs hosted by the dacites, magnesio-hastingsites with Al^{IV} and Mg# contents similar to those of the G_{11} dacites occur as phenocrysts (Fig. 5c).

The Al^{IV} contents show a range of 1.13–1.43 in the low-Al amphiboles and 1.83–2.41 in the high-Al amphiboles. The two types of amphibole have distinctive Mg# values of 50–71 in the low-Al amphiboles and 67–83 in the high-Al amphiboles. Almost all of the high-Al amphiboles have Mg# values >70, with the majority >75. The Mg# values correlate with both Al_2O_3 and Al^{IV} contents (Fig. 5c). The increasing values of Mg# with Al^{IV} suggest that amphiboles with higher values formed under higher P–T conditions.

Similar to the Mg# vs. Al^{IV} diagram, the low- and high-Al amphiboles plot in two distinct fields on the Al^{VI} vs. Al^{IV} diagram (Fig. 5b), and the discrimination of the two types of amphibole is also confirmed by the classification diagram (Fig. 5a), where the low- and high-Al amphiboles cluster in two distinct fields. In all three diagrams (Fig. 5a, b and c), the high-Al cores that represent antecrysts (samples from the dacites of G_2, and high-silica andesites of G_3 and G_{10}) overlap.

The investigated clinopyroxenes can be classified as augite and diopside according to the IMA classification (Morimoto et al., 1988; Fig. 6a, b).

A single type of clinopyroxene is sometimes encountered (e.g., diopside in G_3 and G_{11} and augite in G_2 and G_5). The clinopyroxene analyses used for the P–T calculations are displayed in Appendix 5 of the Supplementary Data. Selected clinopyroxene analyses are presented in Table 3.

The diopsidic clinopyroxenes have similar narrow compositional ranges ($Wo_{43-48}En_{39-45}Fs_{7-15}$), as do the augites ($Wo_{37-43}En_{35-42}Fs_{17-22}$). In the augites of G_2, G_5, G_7 and G_9, Mg# values are in the range of 59–88, with lower values (59–70) and higher values (72–88) in the diopsides of G_3, G_6, G_{10}, G_{11} and G_{12}. Diopsides from G_{11}, especially those contained in the MMEs hosted by the dacites, exhibit the highest Mg# values (Fig. 6c, d). Most of the analysed clinopyroxenes show low variations in Mg# (e.g., 67–70 in the G_2 dacites/rhyolites, Fig. 4d, and 74–82 in the G_{12} olivine-bearing basalts, Fig. 4f). The maximum Mg# variation (69–79) is recorded in a normally zoned crystal from the G_6 high-silica andesites (Fig. 4e).

The Al_2O_3 and CaO contents of the pyroxenes increase with Mg#, whereas TiO_2 contents show a slight decrease. In Fig. 6d, Cr_2O_3 and Mg# display a positive correlation in the clinopyroxenes from G_3, G_{10}, G_{11} and G_{12}, and a strong enrichment in Cr_2O_3 with increasing Mg# in the clinopyroxenes from G_3 and G_{11}.

4.3. Geothermobarometry

The reliability of P–T data obtained using the different amphibole-based geothermobarometers debated among the scientific community. If the temperature data are generally accepted, the pressure data continue to be disputed because the geobarometers are based on the compositions of magmatic amphiboles, which, as experimental studies show, can be influenced by many factors such as temperature, pressure, melt composition, H_2O content and fO_2. At the same time, recent experimental studies have revealed that during crystallisation the relationships between different factors and amphibole compositions are still controversial. Some researchers have concluded that amphibole composition is directly influenced by pressure (e.g., Blatter et al., 2017; Mutch et al., 2016; Prouteau and Scaillet, 2003), but others consider that temperature is the main factor that determines amphibole composition (e.g., Nandedkar et al., 2016; Ulmer et al., 2018). The amphiboles from volcanic rocks are commonly defined by their Al contents (Al_2O_3/Al^{tot} ratio or Al^{IV}), which are influenced by the P and T of the magma from which they crystallised. The controversial issue is whether high-Al amphiboles (e.g., pargasite, hastingsite, sadanagaite) crystallise at higher pressures, and consequently at greater depths, than low-Al amphiboles.

Using the amphibole barometers developed by Ridolfi et al. (2010) and Ridolfi and Renzulli (2012) for synthetic amphiboles in eleven experimental studies at 2–4 kbar, Erdmann et al. (2014) concluded that high-Al amphiboles can also crystallise at low P. At the same time,

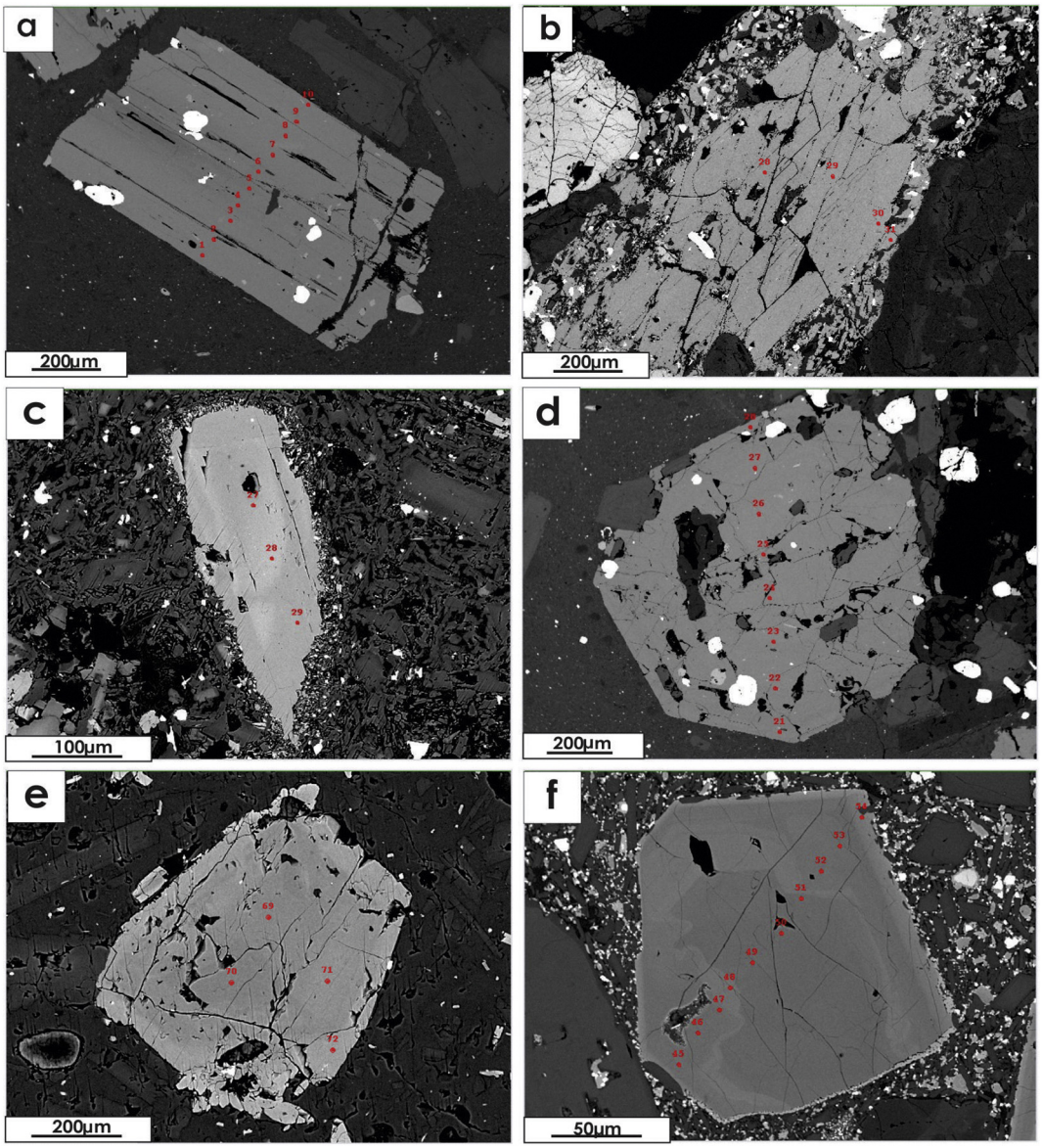

Fig. 4. BSE images of the amphiboles and clinopyroxenes used in the P-T calculations. a. Low-Al amphibole (magnesio-ferri-hornblende) phenocryst (7.68–8.69 Al_2O_3 along a 10 points traverse profile) from the G_2 dacites/rhyolites; b. Low-Al amphibole phenocryst (8.85–9.20 Al_2O_3, magnesio-ferri-hornblende) with thick reaction rim (cpx + plg + Fe-Ti ox) from the G_6 high-silica andesites; c. High-Al amphibole xenocryst (12.49–14.01 Al_2O_3, magnesio-hastingsite) with thin reaction rim (cpx + plg + Fe-Ti ox) from the G_{11} high-silica andesites; d. Unzoned augite xenocryst with Fe—Ti oxides and plagioclase inclusions from the G_2 dacites/rhyolites; e. Normally zoned augite xenocryst from the G_6 high-silica andesites; f. Clinopyroxene (augite) phenocryst with oscillatory zonings in the G_{12} olivine-bearing basalts.

Table 2
Chemical composition of representative amphiboles from the GVZ volcanic rocks.

Volcanic structure	G2	G3	G5	G5aD	G5a MME	G6A	G6D	G10	G11A	G11D	G11 MME	G12
Sample	6001 K 1 05	72FAMF51	36 KBAM1K	52KAMFO3	52KAAMF13	4402E hbl 3 1	54KAMFH5	72KAMF33	10,000 KC 1 01	10,000 KB 3 01	10,011 K hbl 1 4	34KAM12
SiO_2	44.81	45.52	41.44	39.78	38.75	46.15	46.00	40.64	40.93	40.77	41.50	40.97
TiO_2	1.58	1.57	2.35	2.62	2.89	1.74	1.63	2.92	2.69	3.12	2.83	3.38
Al_2O_3	8.69	8.75	13.55	12.89	14.17	7.91	7.36	12.00	14.11	14.21	13.20	13.00
FeO	19.04	16.28	11.17	14.46	12.86	15.66	15.77	14.73	11.26	10.80	10.02	11.83
MnO	0.74	0.40	0.18	0.16	0.13	0.28	0.38	0.23	0.13	0.13	0.16	0.10
MgO	10.49	12.26	14.17	12.30	13.53	12.92	12.77	12.36	14.08	14.23	14.86	13.47
CaO	10.40	11.06	11.51	11.59	11.67	11.20	11.27	11.53	11.39	11.50	11.92	11.70
Na_2O	1.55	1.36	2.31	2.15	2.13	1.38	1.46	1.94	2.07	2.20	2.20	2.27
K_2O	0.59	0.52	0.24	0.33	0.29	0.53	0.53	0.84	0.82	0.78	0.96	0.90
Cr_2O_3	0.02	0.02	0.03	0.01	0.01	0.01	0.03	0.00	0.00	0.01	0.01	0.05
Total	98.10	100.26	99.60	98.95	99.34	100.20	99.63	99.75	99.84	99.83	99.73	99.97

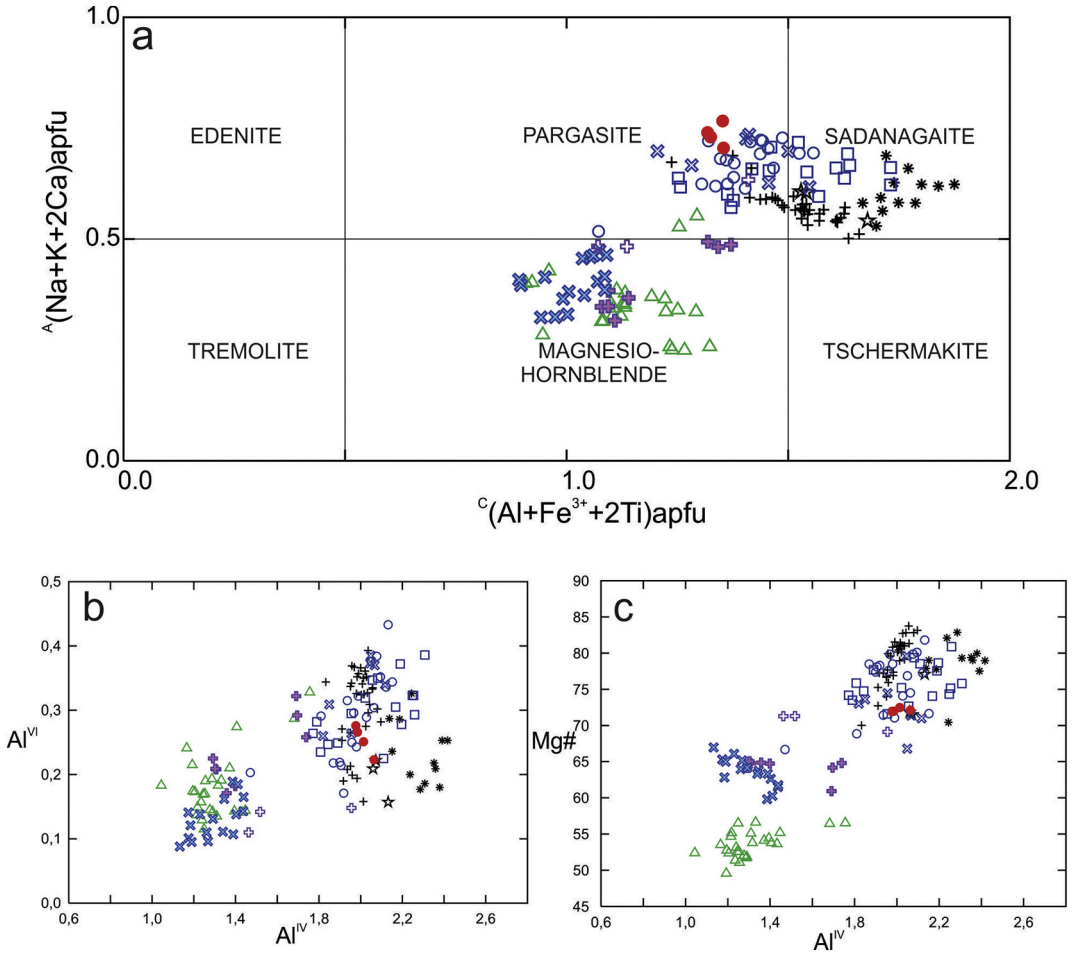

Fig. 5. Chemical features of the amphiboles from the studied GVZ volcanic rocks. (a) Plots of the amphiboles in IMA classification diagram (Hawthorne et al., 2012); (b) Plots of the amphiboles in Al^{VI} vs. Al^{IV} diagram and (c) Plots of the amphiboles in Mg# vs. Al^{IV} diagram. Note the similar fields of variation in the two diagrams of the two types of low- and high-Al amphiboles. Symbols as in Fig. 2.

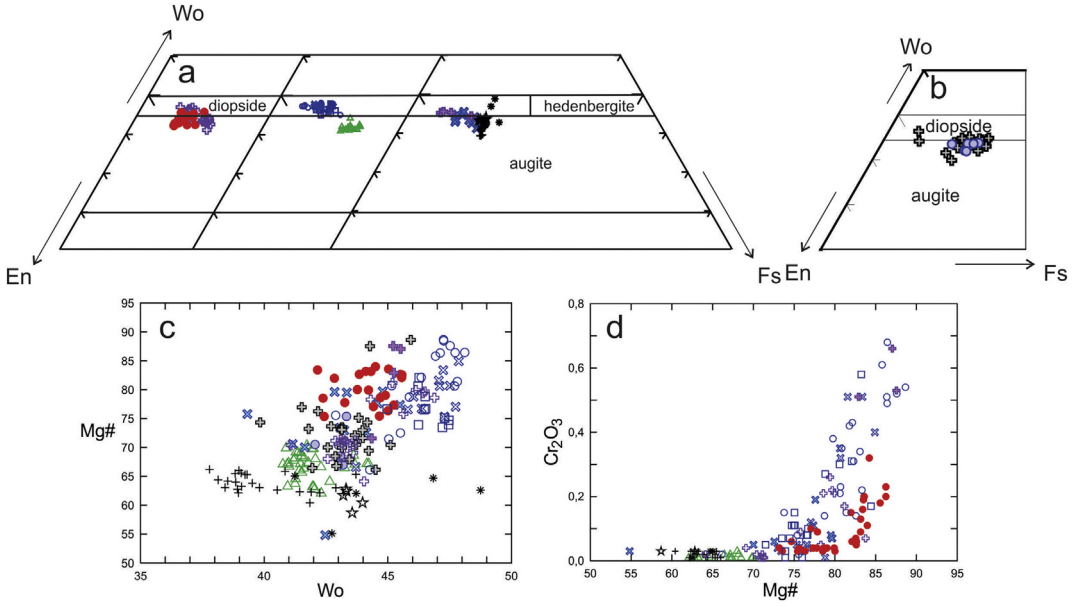

Fig. 6. Pyroxene quadrilateral classification diagrams (Morimoto et al., 1988): a. Clinopyroxenes from the volcanic rocks with both clinopyroxenes and amphiboles; b. Clinopyroxenes from G_7 and G_9 volcanic rocks without amphiboles; Plots of the clinopyroxenes in Mg# vs. Wo (c) and Cr_2O_3 vs. Mg# (d) diagrams. Wo - wollastonite. Symbols as in Fig. 2.

Table 3
Chemical composition of representative clinopyroxenes from the GVZ volcanic rocks.

Volcanic structure	G2	G3	G5	G5aD	G5a MME	G6	G7	G9	G10	G11A	G11D	G11 MME	G12
Sample	6001 K 1 03	72F CPX23	36 KB CPX2A	53 K CPXI2	52KA CPX24	4402E cpx 1 3	10,002 K cpx 1 2	1600E cpx 3 6	25,899 K 1 03	10,000 K C 1 04	10,000 KB 4 03	10,004 K 2 02	10,013 K 1 05
SiO_2	51.77	51.09	50.15	51.74	50.28	50.97	51.70	49.24	49.00	50.76	48.62	50.31	50.97
TiO_2	0.41	0.35	0.73	0.29	0.44	0.55	0.46	0.95	1.10	0.62	0.96	0.55	0.65
Al_2O_3	1.90	4.42	3.32	1.36	3.51	3.12	1.78	4.81	6.15	4.09	5.86	4.44	4.53
FeO	12.07	4.41	11.01	10.01	10.41	7.32	10.56	9.23	7.84	5.43	7.56	5.88	5.78
MnO	0.33	0.18	0.41	0.52	0.40	0.21	0.37	0.27	0.15	0.10	0.15	0.13	0.10
MgO	13.18	16.65	13.55	13.97	13.31	15.94	14.09	13.99	13.78	15.30	13.96	15.16	15.37
CaO	19.64	22.57	20.48	21.25	21.10	21.34	21.01	20.93	21.22	22.86	22.04	22.18	21.68
Na_2O	0.27	0.20	0.31	0.26	0.29	0.20	0.24	0.23	0.20	0.19	0.20	0.21	0.20
K_2O	0.01	0.01	0.00	0.00	0.00	0.00	0.00	0.00	0.00	0.00	0.00	0.00	0.02
Cr_2O_3	0.00	0.66	0.00	0.03	0.00	0.08	0.04	0.02	0.09	0.51	0.10	0.43	0.07
Total	99.61	100.88	100.25	99.64	100.01	99.74	100.25	99.67	99.54	99.87	99.45	99.28	99.39

they also indicated that the two models for pressure calculation are untenable. Using the same methodology, Kiss et al. (2014) reached similar conclusions when demonstrating that the high-Al amphiboles (pargasites) in the dacite of the Ciomadul volcano (Eastern Carpathians) were formed at low to medium pressures (3–4 kbar).

Most recent experimental studies have demonstrated that the crystallisation of high-Al amphiboles takes place at high P such as 7 kbar (Nandedkar et al., 2016), 8–10 kbar (Mutch et al., 2016), 7–9 kbar (Blatter et al., 2017) or 10 kbar (Ulmer et al., 2018). The starting materials of the experiments had compositions of basalt, basaltic andesite, tonalite and dacite. High-Al amphiboles had also been obtained at high P (8.3 and 9 kbar) in the earlier experiments of Prouteau and Scaillet (2003), starting with a dacite from Pinatubo volcano. In fact, according to Sato et al. (2005), there is little evidence that high-Al amphiboles crystallise at low-pressure in natural rocks.

The new thermobarometer of Putirka (2016), based on amphibole and melt/liquid equilibrium compositions, solves the main calibration problem of the Ridolfi et al. (2010) and Ridolfi and Renzulli (2012) thermobarometers, which did not account for the influence of the magma/melt composition (a problem also noted previously by Erdmann et al., 2014). Using the thermobarometer of Putirka (2016), we tested some of the new experimental data for amphiboles. To calculate the pressure, we used high-Al amphibole compositions obtained at high P (7–10 kbar) and liquid compositions (corresponding runs or starting materials) from experiments (see Appendix 4, Supplementary Data). The comparative data between the calculated and experimentally acquired pressures draw attention to smaller or greater differences within the P ranges of 0.6–0.9 kbar in Nandedkar et al. (2016), 0.5–2.0 kbar in Blatter et al. (2017) and 0.6–1.6 kbar in Ulmer et al. (2018). However, overall, the differences fall within the standard error of estimate (SEE) = ±1.5–1.7 kbar of Putirka's barometer. The data calculated using the barometers of Ridolfi and Renzulli (2012) and especially Ridolfi et al. (2010) in the worksheet of Putirka (2016) are clearly open to dispute (see Appendix 4, Supplementary Data). In the same way, we also tested the P data for some high-Al amphiboles (pargasites) and a low-Al amphibole (magnesio-hornblende) from Ciomadul volcano published by Kiss et al. (2014). The compositions of two different whole rocks (G_5 basaltic andesite with 54.58 wt% SiO_2 and G_2 dacite with 70.40 wt% SiO_2) were used for the liquid compositions in the P–T calibrations. These compositions satisfy the test of equilibrium in the Putirka (2016) thermobarometer. The results reveal that the pressures calculated with the Putirka (2016) barometer for the high-Al amphiboles are much higher than those calculated by Kiss et al. (2014): 5.9–8.3 kbar in this study vs. 3.9 ± 1 kbar in Kiss et al. (2014) based on Ridolfi et al. (2010) and 3.0 ± 1.2 kbar based on Krawczynski et al. (2012). The low value we calculated for the low-Al amphiboles (1.2 kbar) is similar to the 1.3 ± 0.2 kbar obtained by Kiss et al. (2014). Similar results were attained for the high-Al amphiboles (phenocrysts and megacrysts) and a low-Al amphibole (phenocryst) from Merapi volcano, so the *P* values we obtained for the high-Al amphiboles using the Putirka (2016) barometer ranged from 7.0 to 8.6 kbar, which is markedly higher than the 4.6–5.9 kbar given by the Ridolfi and Renzulli (2012) barometer (Erdmann et al., 2014), while the P values for the low-Al amphibole, using the two barometers, are quite similar (3.2 vs. 2.8 kbar). We also calculated a range of P values (6.7–8.1 kbar) that are similar to those published by Peters et al. (2017) for some other high-Al amphiboles (megacrysts) from Merapi volcano.

We conclude, therefore, that the two distinct compositional types of amphibole (low- and high-Al types), which are present in a wide variety of volcanic rocks (from basalt to rhyolite) in the GVZ study area, allow us to calculate the P–T parameters and assess the nature and locations of the original magma reservoirs. The presence of similar-composition amphiboles in the G_{12} basalts and G_5 basaltic andesites (high-Al macrocrysts) on the one hand, and in the MMEs in the hybrid rocks of the G_{11} dacites and G_5a high silica andesites/dacites on the other also provided a challenge when attempting to determine the magma sources based on P–T calculations.

In addition to our P–T results based on the amphibole barometer of Putirka (2016), we also used clinopyroxene-derived P–T data based on the barometers of Putirka (2008) and Neave and Putirka (2017) to utilise the crystallisation parameters of both the amphiboles and clinopyroxenes (as recommended by Putirka) in our attempt to fully understand the VPS of the GVZ.

4.4. Amphibole thermobarometry

The P–T parameters of amphibole crystallisation were calculated using the thermobarometer of Putirka (2016), which is based on mineral–liquid pairs with inputs of liquids with certain H_2O contents (wt%). The H_2O contents are extremely important, because in this thermobarometer the P given by the amphibole (Eqs. 7a and 7b) increases at a rate of 0.4 kbar per 1 wt% increase in liquid H_2O content. Putirka (2016) noted that water contents are higher at greater pressure, and Eggler (1972) noted that amphibole is only stable for H_2O contents >4 wt%. Moreover, experimental studies showed that >6 wt% H_2O was required to stabilise amphibole in the Montagne Pelée andesite (Martel et al., 1999), and magnesio-hastingsitic amphiboles with >11 wt% Al_2O_3 and Mg# values of 70–84 were produced experimentally by Prouteau and Scaillet (2003) at pressures of 9.6 kbar, under which conditions the H_2O contents of the melt exceeded 10 wt%. Furthermore, Grove et al. (2003) demonstrated experimentally that high-Mg# (>77) amphiboles crystallise early in a magma only when the pressure is high (>5 kbar) and the H_2O content is very high (>10 wt%). In the experiments of Blatter et al. (2017) with Mount St. Helens dacite at 7–9 kbar, amphibole crystallised in runs with 6 and 9 wt% H_2O but was absent in runs with 3 wt% H_2O at near-liquidus conditions. In another

experiment, at a high pressure of 10 kbar, Ulmer et al. (2018) reported that amphiboles crystallised from a liquid of basaltic andesite composition with 7.6 wt% H_2O at 1050 °C, and from a high-Mg basalt composition liquid with 7.3 wt% H_2O at the same temperature. Applying his new thermobarometer to the amphiboles of the Augustine and Merapi volcanic rocks, Putirka (2016) used an H_2O input of 5 wt%. For our P–T calculations we used H_2O inputs of between 4 and 7 wt%, in accordance with the composition of the amphibole (e.g., 4 wt% H_2O for the low-Al low-Mg# amphiboles, and 6–7 wt% H_2O for the high-Al high-Mg# amphiboles).

Whole rock compositions similar to the host GVZ volcanic rocks were used as liquid compositions. The selected compositions were in accordance with the amphibole compositions, and the test of equilibrium Kd (Fe—Mg) = 0.28 ± 11 (Eq. 2 in the Putirka, 2016 thermobarometer) was satisfied. Around 10% of the studied samples exceeded the Kd range by very small values (see Eq. 2 in the worksheet from Appendix 4, Supplementary Data). The predicted SiO_2 content of the liquid required by Eq. 10 in the Putirka (2016) thermobarometer was also considered to be a rough indicator of what the liquid should be (the error = ±4 wt%). The pressures obtained correspond to Eq. 7b (SEE = 1.5 kbar), and the temperatures represent an average of all eight equations of the thermobarometer, with a range of errors of ±28–33 °C. Putirka recommended that the results of Eq. 7b be compared with the results of Eq. 7a for a better pressure estimation. He also argued that if the individually obtained pressure values are averaged using Eqs. 7b and 7a, P can be estimated with an error of ±1 kbar in the 1–8 kbar range.

The calculated P–T data for amphiboles in the GVZ are presented in Table 4 and plotted on Fig. 7a–b. In Table 4, our data, alongside the thermometer data of Molina et al. (2015) and the barometer data of Ridolfi et al. (2010) and Ridolfi and Renzulli (2012), represent averaged values.

The data illustrated in Table 4 display a very strict correlation between pressures, temperatures and Al_2O_3 contents, as well as a good correlation with Mg# and the type of amphibole (high P–T values for magnesio-hastingsite and ferri-sadanagaite and low P–T values for magnesio-ferri-hornblende). Fig. 7a–b shows distinct fields of variation for the two types of amphibole (low- and high-Al), in accordance with the other variation diagrams based on amphibole chemistry (e.g., Al^{VI} vs. Al^{IV} and Mg# vs. Al^{IV} in Fig. 5b–c). There is a remarkable similarity between the patterns of the plotted data in the two diagrams of Fig. 7 with both displaying positive correlations, which in the one case is between pressure and temperature and in the other between pressure and Al^{IV}.

The P and T values for the amphiboles from G_2, G_3, G_6 and G_{10} fall within a narrow range of 0.4–1.8 kbar and 800–860 °C. The higher values correspond to antecrysts (from G_2, G_3 and G_{10}). The amphiboles from G_5, G_{11} and G_{12} have similar P–T data, ranging from 6 to 9 kbar and from 950 to 1010 °C. The amphiboles from the MMEs in G_{5a} have the highest P–T values, which correlate directly with Al contents (Fig. 7a, Table 4). The G_{11} composite dome has similar P–T values for the high-silica andesites and dacites, and also the gabbroic MMEs in the dacites. G_{12} shows consistent values that reflect the homogeneous composition of the single analysed amphibole macrocryst from a basalt.

The P–T data constrain the genetic relationship between the mineral and the host rock. The low-Al amphiboles (7.5–9.3 wt% Al_2O_3) represented by magnesio-ferri-hornblendes are phenocrysts in the high-silica andesites (G_3A, G_6A and G_{10}A), dacites (G_6D) and dacites/rhyolites (G_2D/R; see Table 4). The P–T data for rare cores with high Al contents (11.2–12.0 wt% Al_2O_3) in such crystals (e.g., G_2, G_3 and G_{10}) suggest antecrysts (see Fig. 7a and Table 4). The P–T data for high-Al amphiboles (11.5–15.6 wt% Al_2O_3) represented by magnesio-hastingsites, ferri-sadanagaites and pargasites confirm that they are phenocrysts in the G_{12} basalts, G_5 basaltic andesites, G_{5a} and G_{11} gabbroic MMEs, and xenocrysts in the G_5a/high-silica andesites/dacites, G_{11}A/high-silica andesites and G_{11}D/dacites.

4.5. Clinopyroxene thermobarometry

We used the thermometer and barometer of Putirka (2008) to calculate the pressures and temperatures of clinopyroxene crystallisation in the GVZ. For these clinopyroxene–liquid thermobarometers, a test of the equilibrium between clinopyroxene and the selected liquid is the Fe—Mg exchange coefficient or $K_D^{cpx-liq}$, which should be 0.27 ± 0.03 (BH column and Eq. 35/BT column in the worksheet for P–T calculations, Appendix 5, Supplementary Data). Another—perhaps better—test recommended by Putirka (2008) is to compare the predicated and observed values of clinopyroxene components (e.g., diopside and hedenbergite, the DiHd component). Neave and Putirka (2017) refined the Putirka (2008) barometer and demonstrated that those equations based exclusively on clinopyroxene compositions (Eqs. 32a, 32b, and especially 32c) are not accurate at lower pressures. They mentioned that Eq. 32c, which has been used by many authors, is accurate only at pressures of >7 kbar. In their application, they filtered the clinopyroxene–liquid pairs taking into consideration values within 10% Fe—Mg

Table 4
Averages of the calculated temperatures and pressures of crystallisation for the studied amphiboles. n – number of analyses; B - basalts; BA - basaltic andesites; A - andesites; D - dacites; D/R - dacites/rhyolites; MME - mafic microgranular enclaves; TiMgHast, MgHast - Ti-rich magnesio-hastingsite, Magnesio-hastingsite; TiFeSadan, FeSadan - Ti-rich ferri-sadanagaite, Ferri-sadanagaite; MgFeHbl - Magnesio-ferri-hornblende; phenocr - phenocrysts; xenocr - xenocrysts; antecr - antecrysts; 1a,1e – Ridolfi and Renzulli (2012) geobarometers used to calculate the amphiboles pressures.

No	Volcanic complex	Rock type	Amphibole type	Mg # (average)	Al_2O_3 (average)	Temperature (°C)		Pressure (Kbars)		
						Putirka (2016)	Molina et al. (2015)	Putirka (2016)	Ridolfi et al. (2010)	Ridolfi and Renzulli (2012)
1	G_{12}	B	TiMgHast (phenocr)	72.1 (n = 4)	13.00	994	958	7.8	3.3	7.3 (1e)
2	G_{11}	A	TiMgHast (xenocr)	72.9 (n = 7)	13.37	978	962	7.4	3.6	7.7 (1e)
		D	MgHast (xenocr)	75.9 (n = 17)	13.77	981	960	7.5	3.8	7.0 (1e)
		MME	TiMgHast (phenocr)	76.4 (n = 19)	13.26	983	958	7.3	3.3	7.5 (1e)
3	G_{10}	A	TiMgHast (antecr)	69.1 (n = 1)	12.00	940	914	4.4	2.7	4.7 (1e)
			MgFeHbl (phenocr)	71.2 (n = 2)	9.34	888	907	1.6	1.4	1.7 (1a)
4	G_6	A	MgFeHbl (phenocr)	62.7 (n = 11)	8.53	848	889	1.2	1.2	1.3 (1a)
		D	MgFeHbl (phenocr)	65.1 (n = 6)	7.58	840	886	0.7	1.0	1.0 (1a)
5	G_5	BA	FeSadan (phenocr)	79.1 (n = 35)	13.35	978	957	7.6	3.5	6.7 (1e)
	a	D	FeSadan (xenocr)	73.5 (n = 3)	13.04	950	914	5.9	3.4	5.3 (1e)
		MME	TiFeSadan (phenocr)	78.7 (n = 12)	14.50	990	960	8.4	4.5	6.0 (1e)
6	G_3	A	MgFeHbl (antecr)	63.3 (n = 3)	11.40	906	921	3.7	2.4	4.3 (1e)
			MgFeHbl (phenocr)	64.7 (n = 5)	8.76	842	887	1.5	1.3	1.2 (1a)
7	G_2	D/R	MgHast (antecr)	56.4 (n = 2)	11,50	878	884	3.6	2.4	5.4 (1e)
			MgFeHbl (phenocr)	53.3 (n = 25)	8.01	815	886	0.8	1.2	1.6 (1a)

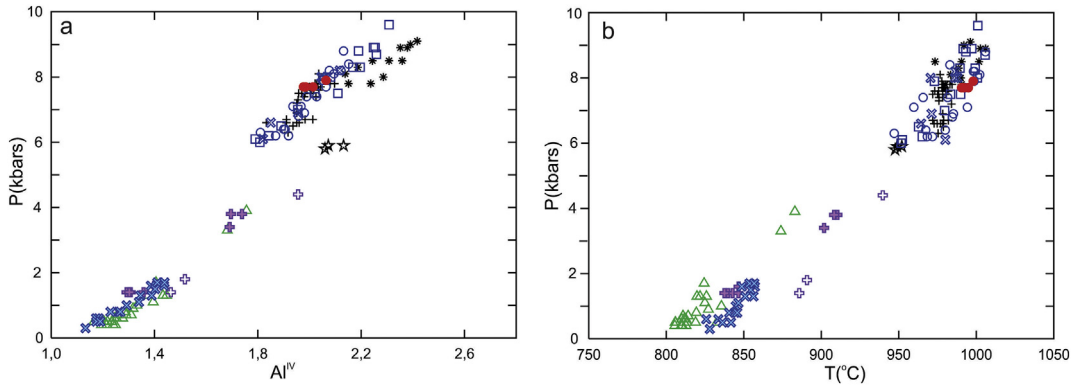

Fig. 7. Pressure vs Al^{IV} (a) and pressure vs temperature (b) diagrams of the GVZ amphiboles, calculated using Putirka (2016) geothermobarometers. Note the distinct plotting fields for the low- and high-Al amphiboles, corresponding to low and respectively high pressures. Antecrysts from G_2 dacites and from G_3 and G_{10} high-silica andesites plot in between the two main fields. Symbols as in Fig. 2.

equilibrium (Eq. 35) and within 20% of DiHd component equilibrium. In our calculations, the clinopyroxene–liquid pairs were selected within the 10% of DiHd component equilibrium values using a one-to-one line diagram (Fig. 8a) and matching 0.27 ± 0.03 $K_D^{cpx-liq}$ (Eq. 35) values. The pressures were calculated using Eq. 31 (SEE = ±2.9 kbar) and the temperatures given by Eq. 33 (SEE = ±45 °C) in the Putirka (2008) models. The calculated P–T data are plotted in the P–T diagram of Fig. 8b and listed as average values in Table 5.

The P–T clinopyroxene calculations have been extended to two additional volcanic structures, G_7 and G_9. The P–T diagram (Fig. 8b) displays generally positive correlations, mainly for the clinopyroxenes from G_2, G_5, G_6, G_7 and G_{10}. The clinopyroxenes from G_{12} and G_3 plot in distinct fields due to the higher T values (Fig. 8b). The P–T data for the clinopyroxenes from G_{12} (Cpx + Ol basalts) are similar to those of the intracaldera basalts (7–8 kbar and 1050 °C) from Los Humeros Caldera (Mexico, Lucci et al., 2020). Overall, *P* values are in the range of 3.5–8.5 kbar and T values in the range of 1050–1150 °C. This T interval corresponds to the temperature of clinopyroxene crystallisation in the high pressure (10 kbar) experiments of Ulmer et al. (2018), which started with a high-Mg basalt composition. The majority of the studied clinopyroxenes plot in the same field of $P > 5$ kbar, and the clinopyroxenes of G_{11} gave the highest P values (7–9 kbar). The high values of pressure and temperature suggest that all the clinopyroxenes from the high-silica andesites and dacites in G_2, G_3, G_{5a}, G_6, G_9, G_{10} and G_{11}A, D represent xenocrysts from basic magmas that were involved in the mixing and mingling processes that generated these hybridised rocks (see Table 5). The calculated P–T data for the amphiboles and clinopyroxenes indicate that the clinopyroxenes crystallised at higher temperatures than the amphiboles in all of the studied volcanic structures (Table 5).

In several high-silica andesites and dacites with clinopyroxene xenocrysts (e.g., G_2, G_3 and G_6), the data show a difference of 220–260 °C in crystallisation temperature between the low-Al amphiboles (magnesio-ferri-hornblendes) and the clinopyroxenes. In these rocks, the amphiboles and clinopyroxenes crystallised at pressures that were also markedly different (by 4–5 kbar). In G_5, G_{11} and G_{12}, where the amphiboles and clinopyroxenes were in equilibrium, a smaller temperature difference of 90–140 °C is recorded (Table 5 and Fig. 9b).

These data correspond with the experimental data of Grove et al. (2003), who postulated that the clinopyroxene crystallised at >100 °C higher than the temperature of the melt in equilibrium with amphiboles. Putirka (2016) also observed a difference of 100–150 °C in the crystallisation temperatures of amphiboles and clinopyroxenes in the Augustine and Merapi volcanic rocks. Similar data were acquired in the recent high pressure (10 kbar) experiments of Ulmer et al. (2018) where clinopyroxene crystallised at ~1200 °C, and amphibole at ~1050 °C, by fractional crystallisation, but at ~1200 °C and ~ 1060 °C,

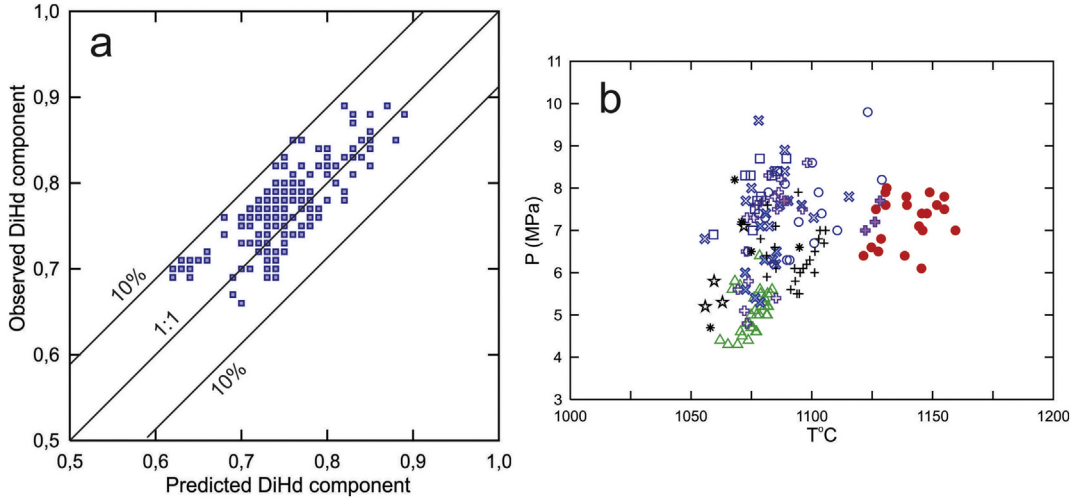

Fig. 8. Mineral DiHd equilibrium tests for GVZ clinopyroxenes (a) and pressure vs. temperature diagram (b), calculated using Putirka (2008) and Neave and Putirka (2017) geothermobarometers. The P-T diagram displays a general positive correlation except for the G_{12} clinopyroxenes which plot in a distinct field due to the higher T values. Symbols as in Fig. 2.

Table 5
Average values of the calculated temperatures, pressures and corresponding depths for amphiboles and clinopyroxenes from the GVZ volcanic rocks. Mg# - magnesium number (as average); Au - augite; Di - diopside; CrDi - Cr-diopside; pheno - phenocrysts; xeno - xenocrysts; antecr - antecrysts.

No	Volcanic complex	Amphibole (Putirka, 2016)						Clinopyroxene (Putirka, 2008)				
		Rock type	Type	Mg#	T (°C)	P (Kb)	Depth (Km)	Type	Mg#	T (°C)	P (Kb)	Depth (Km)
1	G_{12}	B	TiMgHast (pheno)	72	994	7.8	29	Au + Di (pheno)	80	1130	7.0	26
2	G_{11}	A	TiMgHast (xeno)	73	978	7.4	27–28	CrDi (xeno)	80	1070	7.5	27–28
		D	MgHast (xeno)	76	981	7.5	28	CrDi (xeno)	77	1065	7.6	27–28
		MME	TiMgHast (pheno)	76	983	7.3	27	CrDi (pheno)	85	1080	7.1	26–27
3	G_{10}	A	TiMgHast (antecr)	69	940	4.4	16	Au + Di (xeno)	77	1070	6.6	24
			MgFeHbl (pheno)	71	888	1.6	5–6					
4	G_9	A + D						Au + Di (xeno)	67	1070	5.0	18–19
5	G_7	A						Au (pheno)	69	1055	4.2	14
6	G_6	D	MgFeHbl (pheno)	63	848	1.2	4–5	Au + Di (xeno)	75	1070	6.2	23
				65	840	0.7	2–3					
7	G_5	BA	FeSad (pheno)	79	978	7.6	28	Au (pheno)	64	1090	6.3	23–24
		a D	FeSad (xeno)	74	950	5.9	22	Au (xeno)	62	1060	5.4	20–21
		MME	TiFeSad (pheno)	79	990	8.4	31	Au + Di (pheno)	64	1075	6.7	25
8	G_3	A	MgFeHbl (antecr)	63	906	3.7	13–14		83			
			MgFeHbl (pheno)	65	842	1.5	5–6	CrDi (xeno)		1100	7.0	25–26
9	G_2	D/R	MgHast	56	878	3.6	12–13		67			
			MgFeHbl (pheno)	53	815	0.84	3	Au (xeno)		1070	5.0	18–19

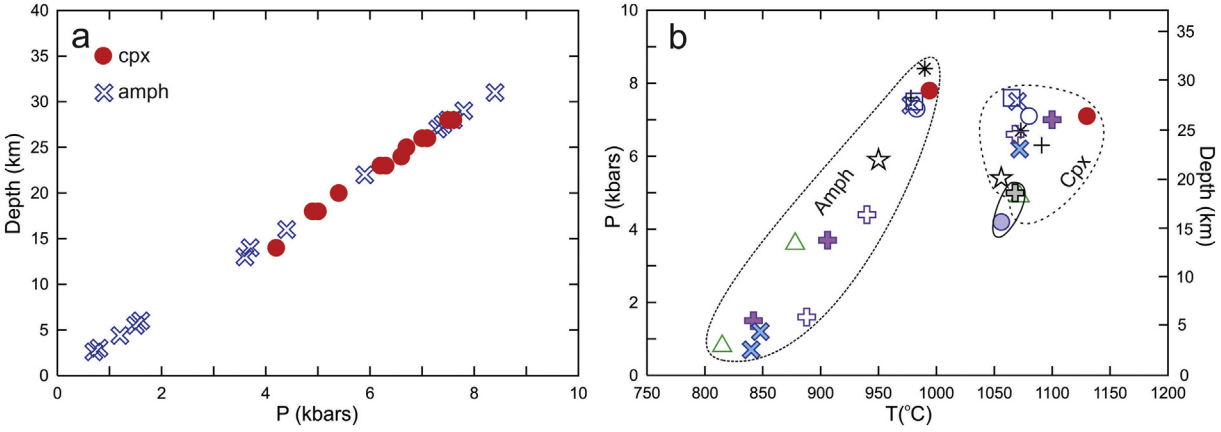

Fig. 9. Pressure vs depth (a) and pressure vs temperature vs depth (b) diagrams for the amphiboles and clinopyroxenes of the GVZ volcanic complexes. The plotted data represent averages of the calculated P and T. Note that the majority of clinopyroxenes and the high-Al amphiboles crystallise at similar depths; dotted outline for the fields of amphiboles and clinopyroxenes from G_2, G_3, G_5, G_6, G_{10}, G_{11} and G_{12}, and solid outline for the field of clinopyroxene from G_7 and G_9. Symbols as in Fig. 2.

respectively, by equilibrium crystallisation, starting with a high-Mg basalt composition. Starting with a basaltic andesite composition, the crystallisation temperature of the clinopyroxene was the same (~1200 °C), and that of the amphibole was ~1080 °C. At ~950 °C, the clinopyroxene coexisted with the amphibole as liquidus phases in both experiments. The pressures of the amphiboles and clinopyroxenes from G_5, G_{11} and G_{12} are in agreement with these experimental data, and similar P data were obtained for the andesites and dacites as well as the gabbroic enclaves hosted by the dacites in G_{11} (Table 5 and Fig. 9b).

4.6. Pressure–depth relationships and implications for the volcanic plumbing systems

The calculated pressures of amphiboles and clinopyroxenes allow us to calculate their crystallisation depths. To do this, we used a density of 2.700 kg/m^3 to represent the average crustal density in the GVZ based on the data of Dererova et al. (2006) regarding the density structure of the continental lithosphere of the Eastern Carpathians: Neogene sedimentary cover, 2400–2550 kg/m^3; Paleogene flysch deposits, 2550–2650 kg/m^3; Neogene volcanics, 2600–2800 kg/m^3; Carpathian–Pannonian upper crust, 2740–2750 kg/m^3; Carpathian–Pannonian lower crust, 2930 kg/m^3. The average values of the depths calculated from the average values of the pressures for the amphiboles and clinopyroxenes are presented in Table 4 and Fig. 9a. The amphibole phenocrysts (magnesio-ferri-hornblendes) from G_2, G_3, G_6, and G_{10} crystallised at shallow depths in the upper crust, whereas the clinopyroxenes (augite and diopside) crystallised in much deeper magma reservoirs, mostly in the lower crust (Fig. 9b, Table 5). Based on the P data, the amphiboles and clinopyroxenes from G_5, G_{11} and G_{12} crystallised at even deeper levels.

The P–T–depth diagram (Fig. 9b) displays different fields of variation for the analysed amphiboles and clinopyroxenes. The diagram indicates different conditions of crystallisation for the acidic rocks of G_2, G_3, G_6 and G_{10}, so the amphibole phenocrysts crystallised at shallow depths (2–6 km), whereas the clinopyroxenes crystallised at depths ranging from 18 to 26 km. The amphibole antecrysts in G_2, G_3 and G_{10} crystallised at depths of 12–16 km. The amphiboles and clinopyroxenes from G_5, G_{11} and G_{12} crystallised at depths of 25–33 km. The clinopyroxenes from G_7 and G_9 crystallised at much shallower levels (14–19 km) than the clinopyroxenes from other volcanic structures.

Based on the depths of crystallisation inferred from the calculated pressures of the investigated amphiboles and clinopyroxenes, four different magma sources can be constrained: 1) very deep sources

(generally >25 km and down to 33 km depth) for the G_3 clinopyroxenes and the G_5, G_{11} and G_{12} amphiboles and clinopyroxenes; 2) deep crustal sources (18–23 km depth) for the G_2, G_6 and G_{10} clinopyroxene xenocrysts and G_9 clinopyroxene phenocrysts; 3) mid-crustal sources (10–15 km depth) for the G_2, G_3, and G_{10} amphibole antecrysts and G_7 clinopyroxene phenocrysts; and 4) shallow sources (2–6 km) for the G_2, G_3, G_6 and G_{10} amphibole phenocrysts. These depth determinations indicate that a complex array of intracrustal magma reservoirs made up the magmatic plumbing systems of the volcanic structures.

4.7. Volcanic plumbing system architecture and its influence on magmatic processes and evolution of volcanism

To characterise the magmatic plumbing systems of the studied volcanic structures in the GVZ, we used the terminology of Cashman et al. (2017) and Sparks et al. (2019). The term *magma reservoir* represents the domain within the magmatic system that contains melt (± fluid), which by definition is above the solidus, and the magma reservoir includes both crystal-dominated and melt-dominated domains. The melt-dominated domain is the *magma chamber* and the crystal-dominated domain is the *mush*. Magma reservoirs consist of magma and mush domains. The reservoir may contain regions of very low fraction intergranular melt, partially molten rock (mush) and melt lenses (or magma chambers) comprising high melt fraction eruptible magma, as well as pockets of exsolved magmatic fluids.

Besides the existence of magma reservoirs constrained by the P–T data, the presence of other shallow-level magma reservoirs is suggested by the mineralogical–petrographical features of the rocks encountered in the studied volcanic structures. The high-silica andesites and dacites from G_2, G_9, G_{10} and G_{11} contain quartz, biotite and Ab-rich plagioclase phenocrysts, as well as amphiboles and clinopyroxenes. In equilibrium crystallisation experiments, quartz appears first at 750 °C under H_2O-saturated conditions in dacite (Scaillet and Evans, 1999) and between 790 and 825 °C at pressures of 1.3–2.0 kbar in andesite (Rutherford and Devine, 2003). Based on these experimental data we suggest a shallow magma source (4–7 km depth) for G_9 and G_{11} that did not contain low-Al amphibole. The presence of biotite and quartz in the G_2 and G_{10} dacites and high-silica andesites supports the existence of shallow crustal magma reservoirs, as constrained by the P–T data for the low-Al amphiboles (magnesio-ferri-hornblendes). Moreover, it has been established in many volcanoes that a mineral assemblage of quartz, biotite and Ab-rich plagioclase represents the final stage of acidic rock crystallisation at shallow crustal levels (e.g., the Cerro Machín volcano of the Colombia dacites, Laeger et al., 2013).

In G_2, G_9, G_{10} and G_{11}, magma mixing between mafic and intermediate magmas and evolved/silicic magmas was an important process (Kovacs, 2002; Kovacs et al., 2017; Kovacs and Fülöp, 2005, 2010), and this implies the existence of shallow-level magma reservoirs, with evolved melt lenses/magma chambers or mushes, in which the magma mixing took place.

The MOHO in the region of the GVZ is constrained to a depth of 33–35 km (Bielik et al., 2018; Săndulescu et al., 1993), and the boundary between the upper and lower crust in the Eastern Carpathians varies between depths of 17 and 21 km (Dererova et al., 2006). Based on this information and our dataset, the magmatic plumbing system of each volcanic structure can be described as follows.

The G_2 composite dome consists of dacites with pyroxenes in the external part of the dome and dacites/rhyolites with biotite + quartz + amphibole + pyroxene in the core of the dome, with the latter hosting diktytaxitic mafic enclaves with elongate amphibole crystals and clinopyroxene clusters. Kovacs and Fülöp (2005) and Kovacs et al. (2017) assigned the two-stage volcanic evolution of the dome to magma mingling and mixing between mafic and silicic melts, based on mineralogical, textural and geochemical features. The calculated pressures for the amphibole phenocrysts (low-Al = 6.9–8.9 wt% Al_2O_3, magnesio-ferri-hornblendes, see Fig. 4a) in the dacite/rhyolite range from 0.4 to 1.7 kbar (average 0.85 kbar), corresponding to crystallisation depths of 1.5–6 km. For the amphibole antecrysts which form the cores of some crystals (11.2–11.8 wt% Al_2O_3, magnesio-hastingsites), the pressures were 3.3–3.9 kbar, suggesting crystallisation at depths of 12–14.5 km. The calculated pressures for the often-clustered clinopyroxenes in the two rock types lie in the range of 4.2–6.3 kbar (average 5.0 kbar), suggesting crystallisation at depths of 16–23 km. We suggest, therefore, a magmatic plumbing system that consisted of at least three magma reservoirs within an array that extended vertically from the upper part of the lower crust to the subsurface (Fig. 10a). The first stage of the volcanism (pyroxene dacite) implies an input of hot basic magma, in which clinopyroxenes had formed by fractionation in the upper part of the lower crust at a temperature of ~1070 °C, and subsequent mixing with an evolved magma in a shallow-level magma reservoir, triggering the first volcanic event. A new deep and hot mafic magma (also constrained by the presence of diktytaxitic amphibole in the mafic enclaves) underwent fractionation in mid-crustal magma reservoirs (clinopyroxenes as xenocrysts and high-Al amphibole as antecrysts) then mingled and mixed with cold silicic magma (T of ~815 °C indicated by the low-Al amphiboles) in the shallow-level magma reservoir. The two populations of amphibole, along with the clinopyroxene xenocrysts, biotite, quartz and Ab-rich plagioclase phenocrysts and the mafic enclaves in the dacites/rhyolites, suggest the existence of a subvertical mush zone as a shallow-level magma reservoir, similar to that described for the dacites of the Ciomadul volcano (Harangi et al., 2015; Kiss et al., 2014; Laumonier et al., 2019). The intrusion of the new hot mafic magma with MMEs and clustered clinopyroxenes reawakened the mush and triggered the second volcanic event, entraining the felsic mush in the eruption (see model of Carrara, 2019).

The Mogoşa composite volcano (Fig. 1b), G_5, includes three representative rock types attributed to three volcanic events: 1) pyroxene basaltic andesite; 2) pyroxene ± amphibole high-silica andesite/dacite (the Valea Morii dome); and 3) pyroxene + amphibole basaltic andesite. Many of the amphiboles in the last volcanic event are macrocrysts. The amphibolitic MMEs (with diktytaxitic texture) are hosted by the high-silica andesites/dacites. All of the amphiboles are high-Al types (12.2–14.0 wt% Al_2O_3 in the basaltic andesites and high-silica andesites/dacites, and 13.8–15.2 wt% Al_2O_3 in the mafic enclaves) with high Mg# values (74–79). The calculated pressures for the amphiboles in the basaltic andesites (G_5) lie in the range of 6.3–8.1 kbar (average 7.6 kbar) suggesting crystallisation took place at depths of 25–30 km (average 28 km). The calculated pressures for the amphiboles in the high-silica andesites/dacites (G_{5a}) are around 5.9 kbar, indicating a shallower crystallisation depth (21–22 km). The highest pressures, 7.8–9.0 kbar (average 8.4 kbar), were indicated by the amphiboles of the diktytaxitic mafic enclaves in the high-silica andesites/dacites (G_{5a}MME), indicating deeper crystallisation depths of 29–33 km. For the clinopyroxenes in the pyroxene basaltic andesites (the first volcanic event) and the amphibole-bearing basaltic andesites and mafic enclaves hosted by the high-silica andesites/dacites, the calculated pressures range from 5.5 to 7.5 kbar, indicating a crystallisation depth range of 21–28 km (average 24 km). Slightly lower pressures were given by the clinopyroxenes in the high-silica andesites/dacites (4.6–6.9 kbar, average 5.4 kbar), suggesting the same deep crustal source (18–26 km, average 21–22 km) as the coexisting amphiboles.

Based on the P–T data and the main features of the volcanic rocks, two models can be built for the Mogoşa volcano (G_5) plumbing system. The first model has a main, very deep crustal magma reservoir system overlain by a smaller upper crustal magma reservoir. Primary mafic magmas that originated in the lithospheric mantle stalled and partially fractionated in the deep lower crustal magma reservoirs and subsequently rose to the surface, erupting as pyroxene basaltic andesites in the first volcanic event (11.4–10.3 Ma, 1 in Fig. 10b). A new mafic melt from the deepest part of the lower crustal magma reservoir then disrupted amphibole-bearing cumulates (the diktytaxitic MMEs),

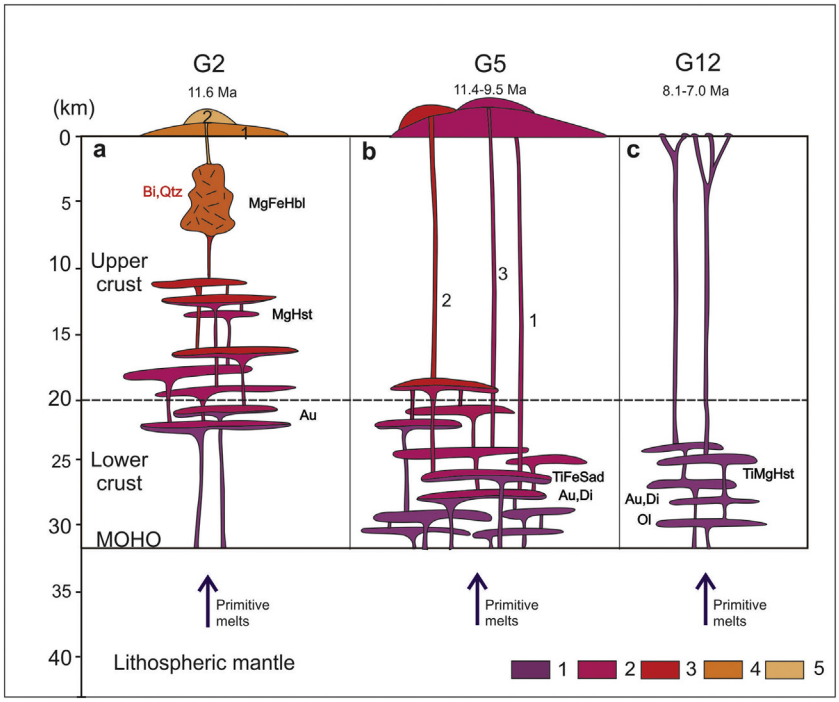

Fig. 10. Schematic representation of the magmatic plumbing systems of the G_2, G_5 and G_{12} volcanic complexes. G_2 (Dăneşti composite dome) with a two stage volcanic evolution associated with magma-mingling and -mixing processes which took place in a subvertical mush zone representing a shallow level magma reservoir: 1. Pyroxene- bearing dacites; 2. Biotite+quartz+amphibole+pyroxene dacites/rhyolites (11.6 Ma); G_5 (Mogoşa composite volcano): 1. Pyroxene basaltic andesites (11.4–10.3 Ma); 2. Pyroxene±amphibole high-silica andesites/dacites (Valea Morii associated dome, 10.1 Ma); 3. Pyroxene+amphibole basaltic andesites (9.5 Ma). G_{12} (Firiza magmatic complex) represented by small intrusive bodies (dykes) of pyroxene+olivine aphanitic basalts (8.1–7.0 Ma). Colors legend of the magmas/rocks: 1. Mafic/basaltic; 2. Evolved mafic/basaltic andesitic; 3. Intermediate/andesitic; 4. Acidic/dacitic; 5. Acidic/rhyolitic. MgFeHbl – magnesio-ferri-hornblende; MgHst – magnesio-hastingsite; TiMgHst – Ti-rich magnesio-hastingsite; Au – augite; Di – diopside; Ol – olivine; Bi – biotite; Otz – quartz. The MOHO limit is drawn based on Săndulescu et al. (1993) and Bielik et al. (2018). The upper-lower crust boundary is based on Dererova et al. (2006).

ascended to an upper crustal magma reservoir, mixed with an evolved magma, and possibly triggered the growth of Valea Morii dome (the high-silica andesites/dacites that host MMEs; 10.1 Ma, 2 in Fig. 10b).

Amphiboles with compositions (high-Al, Mg# and Ti and low FeO and MnO) similar to the amphiboles hosted by the Valea Morii high-silica andesites/dacites and their mafic enclaves have been described in the diktytaxitic mafic enclaves within the andesites of the Mt. Lamington volcano (Humphreys et al., 2018). These amphiboles are considered to have crystallised from primitive melts, and their compositions reflect mixing with a dacite melt (~68 wt% SiO_2) that had been produced by the fractionation of amphiboles from the lower crustal mafic melts.

The second model for the crystallisation of the Valea Morii high-silica andesites/dacites is similar to that suggested by Humphreys et al. (2019) for the Mount St. Helens dacites. They demonstrated that the predominant high-Al amphiboles with high Mg# values (65–84), which are similar to those of Valea Morii including those in the MMEs (Mg# = 74–79), are similar to the near-liquidus amphiboles produced in the experiments of Blatter et al. (2017) at 7–9 kbar using the dacites from Mount St. Helens. In their model for the Mount St. Helens plumbing system, Leeman and Smith (2018) describe a deep crustal source region for the dacitic magmas. The generation of dacitic liquids in equilibrium with high-Al, high-Mg# amphiboles in the lower crust (20–35 km) from basic melts, as constrained by Blatter et al. (2017), was used to explain the genesis of the Mount St. Helens dacites from mafic magmas by AFC processes (Wanke et al., 2019), and we also suggest this as a second alternative model for the Mogoşa volcano (Fig. 10b).

Mafic melts from a deep zone containing gabbroic cumulates generated the pyroxene + amphibole basaltic andesites in the last volcanic event of Mogoşa volcano (9.5 Ma, 3 in Fig. 10b). The amphibole macrocrysts in these lavas were probably derived from mafic cumulates formed in the deepest magma reservoir near the mantle–crust boundary, much the same as for the compositionally similar amphibole megacrysts in the Merapi volcano (Chadwick et al., 2013; Peters et al., 2017). The long-lasting volcanic activity of the Mogoşa volcano (11.4–9.5 Ma), and its remarkable petrographical and geochemical homogeneity (except Valea Morii dome), suggests that the deep, multi-level magmatic plumbing system was continuously replenished with mafic magma from the lithospheric mantle.

A different and much simpler magmatic plumbing system is suggested for the G_{12} intrusive phase (pyroxene + olivine basalts with rare amphibole macrocrysts), which marked the end of volcanic activity in the GVZ (Fig. 10c). The high pressures calculated for the Ti-rich magnesio-hastingsite (~7.8 kbar) and for the diopside and augite (6.1–8.0 kbar), indicate crystallisation in the deep crust (23–30 km depth). The presence of olivine with the high-pressure clinopyroxene confirms the origin of these basalts from a deep magma reservoir. The mafic magma from this reservoir rapidly ascended through the upper crust and intruded the older volcanic rocks of G_6 and G_7. The high-Al amphibole macrocrysts in the basalts possibly originated as mafic cumulates at the bottom of the deepest magma reservoir, similar to Merapi volcano (Peters et al., 2017).

G_3, G_6 and G_{10} consist of high-silica andesites (G_3 and G_{10}) and high-silica andesites and dacites (G_6), which suggests magmatic plumbing systems with an architecture similar to that of G_2 (Fig. 11). This would involve shallow level magma reservoirs (2–7 km depth) indicated by the pressures for the amphibole phenocrysts (and confirmed by the presence of quartz in G_3 and quartz + biotite in G_{10}), mid-crustal magma reservoirs (13–16 km depth) where amphibole antecrysts crystallised, and deep crustal magma reservoirs (20–29 km depth), constrained by the crystallisation of the clinopyroxene xenocrysts (Fig. 11). The VPS of G_9 consisted of mid-crustal magma reservoirs (17–19 km depth) where diopside and augite xenocrysts of the hybrid

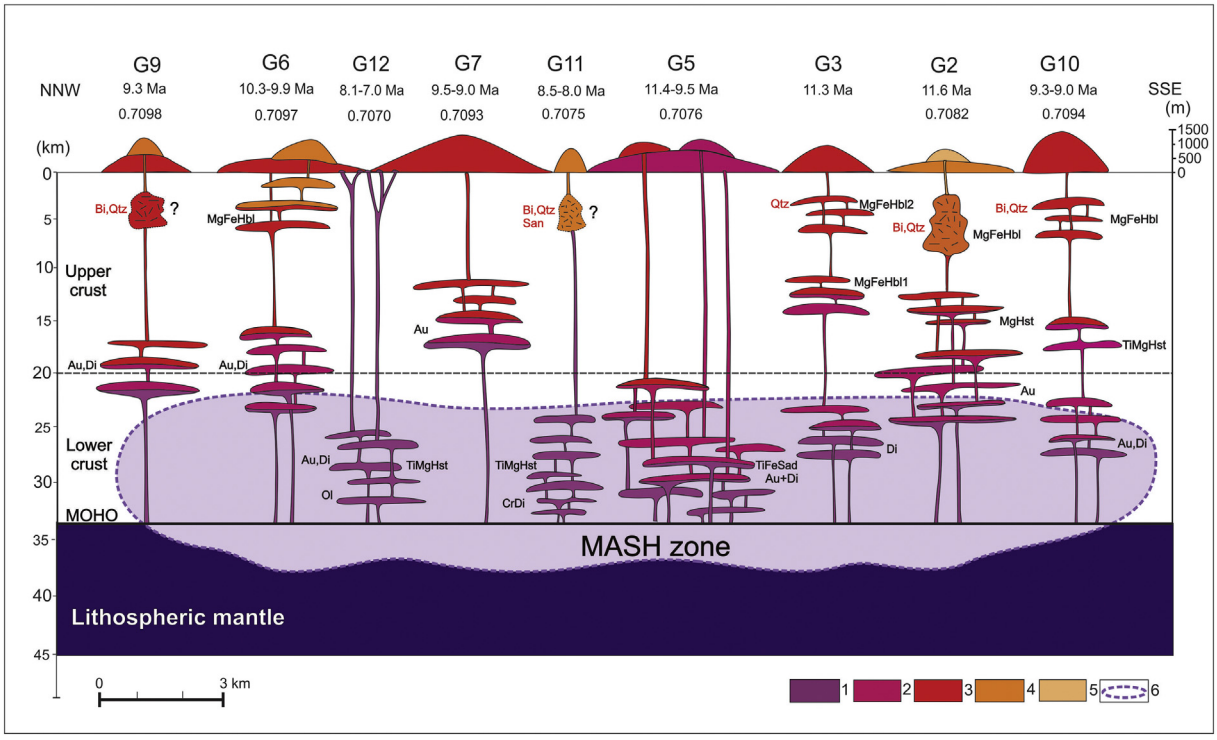

Fig. 11. Conceptual architecture of the magmatic plumbing systems underneath the investigated volcanic structures of GVZ along a NNW-SSE profile. The relative heights and spatial distribution of the volcanic structures are represented at scale. The shallow level magmatic reservoirs of G_9 and G_{11} represent mushy reservoirs inferred from the mineralogical similarity with the volcanic rocks of G_2 composite dome (for which has been constrained such a magmatic reservoir based on the P-T data). Colors legend: 1–5 as in Fig. 10; 6. The assumed main deep magma reservoir ("deep hot zone") that acted as a "MASH zone"; San – sanidine; CrDi – Cr-diopside; The other abbreviations similar with those from Fig. 10; 10.3–9.9 Ma = K-Ar age of the volcanic activity; 0.7076 = $^{87}Sr/^{86}Sr$ ratios of the volcanic rocks from the studied volcanic structures.

acidic rocks crystallised, and a supposed shallow-level magma reservoir (probably a mushy magma reservoir) where biotite and quartz phenocrysts crystallised from a much-evolved colder magma.

G_{11} is composed of a core of dacites that host numerous amphibole-rich gabbroic MMEs and an envelope of high-silica andesites. Similar calculated pressures of 6–9 kbar (average 7.1–7.6 kbar) for the amphiboles and clinopyroxenes in all three lithologies were obtained, suggesting similar deep sites of crystallisation (23–33 km) from mafic magmas. As a result, the deep part of the G_{11} magmatic plumbing system is quite similar to that of the G_{12} intrusive phase. The upper crustal magma reservoirs suggested for G_{11} are consistent with magma mingling and mixing processes involved in their genesis, constrained by the mineralogical, textural and geochemical data (Kovacs, 2002; Kovacs et al., 2017; Kovacs and Fülöp, 2010; Naumov et al., 2014). The deep mafic magmas that intruded the shallow level magma reservoir (possibly a felsic mush) were mixed with highly differentiated and much colder melts to generate the hybrid rocks of G_{11}.

The spatial distribution of the VPS modelled for the nine volcanic structures is illustrated in Fig. 11. The VPS architecture of each volcanic structure has been modelled in accordance with the calculated pressure–temperature data, as well as the mineralogical and textural features of the volcanic rocks. The graphical illustrations in the simplified models shown in Fig. 11 cannot fully follow the new conceptual models of magmatic systems presented by Cashman et al. (2017) and Sparks et al. (2019). In general, each individual VPS is likely to be more complex and more vertically extensive than modelled, with lower crustal magma reservoirs that cannot be constrained with the acquired P–T data, and upper crustal mush zones that are difficult to illustrate in schematic models. We suggest that G_3, G_5, G_{11} and G_{12} originated from very deep magma reservoirs, near the boundary between the lower crust and the lithospheric mantle. Their temporal evolution (from the onset of the G_5 volcanic activity at 11.4 Ma to the end of G_{12} intrusive magmatism at 7.0 Ma) suggests that very deep magma reservoirs could have been active throughout the entire evolution. Uninterrupted volcanism and the spatially close distribution of the volcanic structures with overlapping products suggest the existence of a main magma reservoir at the bottom of the lower crust (Fig. 11). The mid-crustal and shallow level magma reservoirs of the other volcanic structures located in a small area, comparable with that under Etna stratovolcano (Ubide and Kamber, 2018) and only a third wider than that under Ruapehu volcano in New Zealand (Price et al., 2012), could also have their primary sources in this main deep magma reservoir. Consistent with this supposition is that the commonly proposed sources of magma in the GVZ are the lithospheric mantle and lower crust (Kovacs et al., 2017). The large magma reservoir connected to the lithospheric mantle could be seen in the context of the "deep hot zone" of Annen et al. (2006). They defined the deep hot zone as the site of mantle-derived basalt injection and melt generation in the lower crust, between the MOHO and the Conrad discontinuity, which is similar to the suggested main deep magma reservoir beneath the GVZ. A similar unique deep magma reservoir, and a much larger one, is generally acknowledged to occur below the San Diego–Cerro Machín Volcano Tectonic Province of Colombia (Murcia et al., 2019), and this province has volcanological and petrological similarity to the GVZ.

The proposed magmatic plumbing systems can explain the petrological and isotopic features of the GVZ. For example, enhanced crustal contamination characterises the paroxysmal volcanism in the GVZ between 10 and 9 Ma (Kovacs et al., 2017). G_6, G_7, G_9 and G_{10} were generated during this stage, and they are characterised by high values of $^{87}Sr/^{86}Sr$ in the range of 0.7093–0.7098 (Fig. 11). None of these volcanic structures, which involved significant volumes of magma, have any indications of very deep magma reservoirs (constrained by the P–T data), which suggests that the magmas evolved over a long period of time in mid-crustal interconnected magma reservoirs by assimilating

significant amounts of crustal material. On the other hand, the volcanic structures that involved smaller volumes of magma (e.g., G_{11} and G_{12}) are characterised by lower $^{87}Sr/^{86}Sr$ (0.7075 and 0.7070) values, and it seems that the G_{11} and G_{12} magmas that evolved in deep reservoirs did not stall in intermediate crustal reservoirs, but ascended rapidly to the surface, preserving the isotopic signature of the source. Similar $^{87}Sr/^{86}Sr$ (0.7076) values characterise the Mogoşa composite volcano (G_5) where the magma originated in the same deep reservoirs.

The relatively high isotopic signatures (0.7070 and 0.7076 $^{87}Sr/^{86}Sr$) inherited by most basic rocks in the GVZ (e.g., the G_{12} olivine-bearing basalts and G_5 glomerocrystic pyroxene basaltic andesites) suggest crustal contamination in the magma reservoirs took place at the base of the lower crust. This is in accordance with the deep hot zone model of Annen et al. (2006). In their model, this zone represents a mixture of partially-crystallised mantle-derived basalts and partially molten crustal rocks. They argued that partial melting of the lower crust can account for the isotopic signatures of the magmas, similar to the situation described by Hildreth and Moorbath (1988) for MASH zones. Annen et al. (2006) showed that the mantle-derived magmas cannot pass through the deep hot zone without some degree of processing, and this may account for the scarcity of mantle-derived magmas in many volcanic arcs. This means that the absence of lithologies in the GVZ that reflect the composition of the primary magma suggested by Kovacs et al. (2017) may be related to the development of a deep hot zone in the area involving lower crustal melts as well as mantle melts. The absence of primitive lithologies is also a feature of the Rodna–Bârgău subvolcanic area of the Eastern Carpathians, located ca. 100 km away from the GVZ (Fedele et al., 2016).

The VPS proposed here, corroborated by petrographic, geochemical, isotopic and geochronological features of the studied volcanic rocks, indicates that there is an inherent connection between the architecture of the magmatic plumbing system, the petrogenetic processes, and the formation and evolution of the volcanic structures. Thus, the multi-stage volcanic structures with complex mineralogical–petrographical, geochemical and isotopic compositions correspond to more complex types of VPS, as in the cases of G_2, G_3, G_9, G_{10} and G_{11}, which consist of hybrid acidic rocks that involved AFC and magma mingling and mixing processes, and which have multi-level interconnected magma reservoirs extending vertically through almost the entire crust (Fig. 11). In contrast, the compositionally homogeneous volcanic structures correspond to less complex VPS (e.g., the G_7 pyroxene high-silica andesites and the G_{12} olivine-bearing basalts, Fig. 11). The same compositional homogeneity of the G_5 long-lasting basic volcanism is also in accordance with its exclusively deep magma reservoir system (Figs. 10b and 11).

On the scale of the studied area in the GVZ, continuous, long-lasting (~4.5 Myr) volcanism resulted in the emplacement of a wide range of volcanic rocks of different ages, building volcanic structures that constrain the evolution of the intracrustal magmas in complex magmatic plumbing systems. A connection between the supposed "deep hot zone" and a lithospheric mantle source was maintained continuously, as shown by the very deep magma reservoirs feeding the lithospheric mantle in both the youngest (G_{11} = 8.5–8.0 Ma and G_{12} = 8.0–7.0 Ma) and oldest (G_5 = 11.4 Ma and G_3 = 11.3 Ma) volcanic structures. The contemporaneous volcanic events with different magma compositions in the various volcanic structures (e.g., G_2 Bi + Qtz dacites/rhyolites 11.6 Ma, G_5 Px basaltic andesites 11.4 Ma and G_3 Px + Amph high-silica andesites 11.3 Ma, Fig. 1b) can be better understood based on the inferred VPS architectures (Fig. 11). The involvement of magmas with such different compositions in the petrogenesis of the GVZ volcanic rocks can also be explained by the magmatic processes conducted in the deep hot zone. As Annen et al. (2006) argued in their model, evolved melts (hydrous andesitic and dacitic melts) result from the early crystallisation of mantle-derived basaltic magmas with further later crystallisation in the upper crust. Overall, the VPS models proposed here lead to a better understanding of the evolution of volcanism in the GVZ.

5. Conclusions

Eight volcanic structures, composite volcanoes, extrusive domes and an intrusive magmatic complex in the central–southern area of the Gutâi Volcanic Zone (GVZ) were investigated to unravel the architecture of the volcanic plumbing systems (VPS), based on the constrained conditions of amphibole and clinopyroxene crystallisation. Using the currently reliable geothermobarometers of Putirka (2016) for amphiboles, and Putirka (2008) and Neave and Putirka (2017) for clinopyroxenes, P and T parameters were calculated for the amphiboles and clinopyroxenes from different rock types (basalts, basaltic andesites, andesites, dacites/rhyolites and MMEs hosted by dacite). All of the data used in our study satisfied the tests of equilibrium of the geothermobarometers. The amphibole and clinopyroxene datasets provide complementary information for the same rock type, and thus enable one to constrain the array of intracrustal magma reservoirs from which they originated, and as a result allows a model of the VPS of the hosting volcanic structure to be constructed.

The data acquired on amphiboles and clinopyroxenes from G_5, G_{11} and G_{12} correlate well, suggesting similar conditions of crystallisation. In contrast, the P–T data for the amphiboles and clinopyroxenes from G_2, G_3, G_6 and G_{10} indicate variable conditions of crystallisation in multi-level magma storage reservoirs.

The P–T results for the GVZ volcanic rocks are in full agreement with recent experimental studies on the crystallisation of amphiboles and clinopyroxenes (Blatter et al., 2017; Nandedkar et al., 2016; Ulmer et al., 2018). Although the reliability of amphibole barometry remains a matter of debate, new experimental data must be reported.

The different crystallisation depths for the various amphiboles and clinopyroxenes, as constrained by the P–T data, indicate magma sources scattered throughout the entire crust, from near the crust and lithospheric mantle boundary to shallow levels beneath the volcanic structures. Most of the studied volcanic structures have complex, multi-level, interconnected VPS. G_{12} and G_5 consist exclusively of basalts and basaltic andesites with pressure indications of very deep lower crustal magma reservoirs. The volcanic structures formed by hybrid high-silica andesites and dacites via magma mixing and mingling processes (G_2, G_3, G_9, G_{10} and G_{11}) have complex VPS with additional shallow level crustal reservoirs (including mushy magma reservoirs).

The existence of a very deep magma reservoir for several of the volcanic structures, indicating the involvement of lithospheric mantle over the entire time-interval of the volcanism, and which is consistent with the high isotopic signatures of even the most basic rocks, suggests there was a main, deep magma reservoir within a "deep hot zone" (as in the concept of Annen et al., 2006) that functioned as a "MASH zone" at the crust–mantle boundary beneath the GVZ.

The complex VPS architecture revealed in the GVZ played a major role in controlling the petrogenetic processes, leaving their mark on the geological features of the volcanic structures. The existence of intricate volcano plumbing systems also helps to explain the complex and long-lasting volcanism in the relatively small area we studied in the GVZ. As already suggested by Kovacs et al. (2017), the ~7 Myr record of lithospheric mantle melting below the GVZ, which produced a complex intracrustal magma reservoir system, may eventually be seen as part of a fragmentary process of lithosphere foundering (Ducea et al., 2013; Murray et al., 2015) during the geodynamic evolution of the GVZ along the southeastern side of the Transcarpathian Basin (e.g., Márton et al., 2007).

In contrast to previous studies, where the subject of VPS architecture has been approached almost exclusively in relation to single active volcanoes, our study encompassed several extinct volcanic structures in an area of complex volcanism. A better understanding of the evolution of magmatic processes in other extinct volcanic areas is generally required, and we hope that our study provides a useful example of some of the approaches that may be used in future research.

Declaration of Competing Interest

The authors declare that they have no known competing financial interests or personal relationships that could have appeared to influence the work reported in this paper.

Acknowledgements

I. Seghedi benefited by a grant of the Ministry of Research and Innovation, CNCS–UEFISCDI, project no. PNIII-P4-ID-PCCF-2016-4-0014, within PNCDI III. The comments from the two reviewers, Yalcin Ersoy and an anonymous one, as the recommendations from the Editor-in-Chief Xian-Hua Li significantly improved the previous version of the manuscript.

Appendix A. Supplementary data

Supplementary data to this article can be found online at https://doi.org/10.1016/j.lithos.2021.106191.

References

Almeev, R.R., Kimura, J.I., Ariskin, A.A., Ozerov, A.Y., 2013. Decoding crystal fractionation in calc-alkaline magmas from the Bezymianny Volcano (Kamchatka, Russia) using mineral and bulk rock compositions. J. Volcanol. Geotherm. Res. 263, 141–171.

Anderson, J.L., Smith, D.R., 1995. The effects of temperature and fO_2 on the Al-in-hornblende barometer. Am. Mineral. 80 (5–6), 549–559.

Andreucci, B., Castelluccio, A., Corrado, S., Jankowski, L., Mazzoli, S., Szaniawski, R., Zattin, M., 2015. Interplay between the thermal evolution of an orogenic wedge and its retro-wedge basin: an example from the Ukrainian Carpathians. Geol. Soc. Am. Bull. 127, 410–427.

Andújar, J., Scaillet, B., Pichavant, M., Druitt, T.H., 2015. Differentiation conditions of a basaltic magma from Santorini, and its bearing on the production of andesite in arc settings. J. Petrol. 56, 765–794.

Andújar, J., Scaillet, B., Pichavant, M., Druitt, T.H., 2016. Generation conditions of dacite and rhyodacite via the crystallization of an andesitic magma. Implications for the plumbing system at Santorini (Greece) and the origin of tholeiitic or calc-alkaline differentiation trends in arc magmas. J. Petrol. 57, 1887–1920.

Annen, C., Blundy, J.D., Sparks, R.S.J., 2006. The genesis of intermediate and silicic magmas in deep crustal hot zones. J. Petrol. 47, 505–539.

Balla, Z., 1987. Tertiary palaeomagnetic data for the Carpatho-Pannonian region in the light of Miocene rotation kinematics. Tectonophysics 139, 67–98.

Barclay, J., Carmichael, I.S.E., 2004. A hornblende basalt from Western Mexico: water-saturated phase relations constrain a pressure–temperature window of eruptibility. J. Petrol. 45 (3), 485–506.

Bielik, M., Makarenko, I., Csicsay, K., Legostaeva, O., Starostenko, V., Savchenko, A., Simonova, B., Dererova, J., Fojtikova, L., Pasteka, R., Vozar, J., 2018. The refined Moho depth map in the Carpathian-Pannonian region. Contributions to Geophysics and Geodesy 48 (2), 179–190.

Blatter, D.L., Sisson, T.W., Hankins, W.B., 2017. Voluminous arc dacites as amphibole reaction-boundary liquids. Contrib. Mineral. Petrol. 172 (5), 27.

Blundy, J.D., Holland, T.J.B., 1990. Calcic amphibole equilibria and a new amphibole-plagioclase geothermometer. Contrib. Mineral. Petrol. 104 (2), 208–224.

Brey, G.P., Kohler, T., 1990. Geothermobarometry in four-phase lherzolites II. New thermobarometers, and practical assessment of existing thermobarometers. J. Petrol. 31, 1353–1378.

Budd, A.D., 2015. Characterising volcanic magma plumbing systems. A tool to improve eruption forecasting at hazardous volcanoes. PhD thesis. ACTA UNIVERSITATIS UPSALIENSIS, UPPSALA.

Buriánek, D., Kropáč, K., 2019. Petrogenesis of Miocene subvolcanic rocks in the Western Outer Carpathians (southeastern Moravia, Czech Republic). J. Geosci. 64, 105–125.

Camejo-Harry, M., Melekhova, E., Blundy, J., Attridge, W., Robertson, R., Christopher, T., 2018. Magma evolution beneath Bequia, Lesser Antilles, deduced from petrology of lavas and plutonic xenoliths. Contrib. Mineral. Petrol. 173. https://doi.org/10.1007/s00410-018-1504-z [77].

Carrara, A., 2019. Numerical modeling of the physical processes causing the reawakening of a magmatic chamber and of the associated geophysical signals. PhD thesis. Université Savoie Mont Blanc.

Cashman, K.V., Sparks, R.S.J., Blundy, J.D., 2017. Vertically extensive and unstable magmatic systems: a unified view of igneous processes. Science 355. https://doi.org/10.1126/science.aag3055 eaag3055.

Chadwick, J.P., Troll, V.R., Waight, T.E., van der Zwan, F.M., Schwarzkopf, L.M., 2013. Petrology and geochemistry of igneous inclusions in recent Merapi deposits: a window into the sub-volcanic plumbing system. Contrib. Mineral. Petrol. 165, 259–282.

Cooper, G.F., Davidson, J.P., Blundy, J.D., 2016. Plutonic xenoliths from Martinique, Lesser Antilles: evidence for open system processes and reactive melt flow in island arc crust. Contrib. Mineral. Petrol. 171, 87. https://doi.org/10.1007/s00410-016-1299-8.

Costa, F., Scaillet, B., Pichavant, M., 2004. Petrological and experimental constraints on the pre-eruption conditions of holocene dacite from Volca'n San Pedro (36_S, Chilean Andes) and the importance of Sulphur in silicic subduction-related magmas. J. Petrol. 45 (4), 855–881.

Crossingham, T.J., Ubide, T., Vasconcelos, P.M., Mallmann, G., 2018. Parallel plumbing systems feeding a pair of Coeval Volcanoes in Eastern Australia. J. Petrol. 59, 1035–1066.

Csontos, L., 1995. Tertiary tectonic evolution of the intra-Carpathian area: a review. Acta Vulcanol. 7, 1–13.

Csontos, L., Nagymarosy, A., Horvath, F., Kováč, M., 1992. Tertiary evolution in the Intracarpathian area: a model. Tectonophysics 208, 221–241.

Dahren, B., Troll, V.R., Andersson, U.B., Chadwick, J.P., Gardner, M.F., Jaxybulatov, K., Koulakov, I., 2011. Magma plumbing beneath Anak Krakatau volcano, Indonesia: evidence for multiple magma storage regions. Contrib. Mineral. Petrol. https://doi.org/10.1007/s00410-011-0690-8.

Dando, B.D.E., Stuart, G.W., Houseman, G.A., Hegedus, E., Brukl, E., Radovanovic, S., 2011. Teleseismic tomography of the mantle in the Carpathian–Pannonian region of Central Europe. Geophys. J. Int. 186, 11–31.

Davis, B.T.C., Boyd, D.R., 1966. The join Mg2Si2O6-CaMgSi2O6 at 30 kilobars pressure and its application to pyroxene from kimberlites. J. Geophys. Res. 71, 3567–3576.

de Leeuw, A., Filipescu, S., Matenco, L., Krijgsman, W., Kuiper, K., Stoica, M., 2013. Paleomagnetic and chronostratigraphic constraints on the Middle to Late Miocene evolution of the Transylvanian Basin (Romania): implications for Central Paratethys stratigraphy and emplacement of the Tisza–Dacia plate. Glob. Planet. Change 103, 82–98.

Dererova, J., Zeyen, H., Bielik, M., Salman, K., 2006. Application of integrated geophysical modeling for determination of the continental lithospheric thermal structure in the eastern Carpathians. TECTONICS 25. https://doi.org/10.1029/2005TC001883 TC3009.

Ducea, M.N., Seclaman, A.C., Murray, K.E., Jianu, D., Schoenbohm, L.M., 2013. Mantle-drip magmatism beneath the Altiplano-Puna plateau, Central Andes. Geology 42, 915–918. https://doi.org/10.1130/G34509.1.

Edelstein, O., Pécskay, Z., Kovacs, M., Bernad, A., Crihan, M., Micle, R., 1993. The age of basalts from Firiza zone, Igniş Mts., East Carpathians, Romania. Revue Roumaine de Géologie Géophysique et Géographie, Serie de Géologie 37, 37–41.

Eggler, D.H., 1972. Amphibole stability in H_2O-undersaturated calc-alkaline melts. Earth Planet. Sci. Lett. 15 (1), 28–34.

Erdmann, S., Martel, C., Pichavant, M., Kushnir, A., 2014. Amphibole as an archivist of magmatic crystallization conditions: problems, potential, and implications for inferring magma storage prior to the paroxysmal 2010 eruption of Mount Merapi, Indonesia. Contrib. Mineral. Petrol. 167 (6), 1–23.

Fedele, L., Seghedi, I., Chung, S.L., Laiena, F., Lin, T.H., Morra, V., Lustrino, M., 2016. Postcollisional magmatism in the Late Miocene Rodna-Bârgău district (East Carpathians, Romania): Geochemical constraints and petrogenetic models. Lithos 266–267, 367–382.

Fülöp, A., 2002. Facies analysis of the volcaniclastic sequence built up above the 15.4 Ma rhyolitic ignimbrites from Gutâi Mts., Eastern Carpathians. Studia Universitatis Babeş-Bolyai, Geologia, Special issue 1, 199–206.

Fülöp, A., 2003. The begining of volcanism in the Gutâi Mts.: Paleovolcanic and paleosedimentological reconstruction. Editura Dacia Cluj-Napoca 134 pp. (in Romanian).

Geiger, H., Barker, A.K., Troll, V.R., 2016. Locating the depth of magma supply for volcanic eruptions, insights from Mt. Cameroon. Sci. Rep. 6, 33629. https://doi.org/10.1038/srep33629.

Gröger, H.R., Fügenschuch, B., Tischler, M., Schmid, S.M., Foeken, P.T., 2008. Tertiary cooling and exhumation history in the Maramures area (internal eastern Carpathians, northern Romania): Thermochronology and structural data. In: Siegesmund, S., Fügenschuch, B., Froitzheim, N. (Eds.), Tectonic Aspects of the Alpine-Dinaride-Carpathian System. Geological Society of London Special Publications vol. 298, pp. 169–195.

Grove, T.L., Elkins-Tanton, L.T., Parman, S.W., Chatterjee, N., Müntener, O., Gaetani, G.A., 2003. Fractional crystallization and mantle-melting controls on calc-alkaline differentiation trends. Contrib. Mineral. Petrol. 145, 515–533.

Hammarstrom, J.M., Zen, E., 1986. Aluminum in hornblende: an empirical igneous geobarometer. Am. Mineral. 71 (11—12), 1297–1313.

Harangi, S., Novák, A., Kiss, B., Seghedi, I., Lukács, R., Szarka, L., Wesztergom, V., Metwaly, M., Gribovszki, K., 2015. Combined magnetotelluric and petrologic constrains for the nature of the magma storage system beneath the Late Pleistocene Ciomadul volcano (SE Carpathians). J. Volcanol. Geotherm. Res. 290, 82–96.

Hawthorne, F.C., Oberti, R., Harlow, G.E., Maresch, W.V., Martin, R.F., Schumacher, J.C., Welch, M.D., 2012. Nomenclature of the amphibole supergroup. Am. Mineral. 97 (11–12), 2031–2048.

Hildreth, W., Moorbath, S., 1988. Crustal contributions to arc magmatism in the Andes of Central Chile. Contrib. Mineral. Petrol. 98 (4), 455–489.

Holland, T., Blundy, J., 1994. Non-ideal interactions in calcic amphiboles and their bearing on amphibole–plagioclase thermometry. Contrib. Mineral. Petrol. 116, 433–447.

Hollister, L.S., Grissom, G.C., Peters, E.K., Stowell, H.H., Sisson, V.B., 1987. Confirmation of the empirical correlation of Al in hornblende with pressure of solidification of calc-alkaline plutons. Am. Mineral. 72, 231–239.

Horváth, F., 1993. Towards a mechanical model for the formation of the Pannonian basin. Tectonophysics 226, 333–357.

Houseman, G.A., Gemmer, L., 2007. Intra-orogenic extension driven by gravitational instability: Carpathian–Pannonian orogeny. Geology 35, 1135–1138.

Humphreys, M.C.S., Zhang, J., Cooper, G.F., Macpherson, C.G., Ottley, C.J., 2018. Identifying the ingredients of hydrous arc magmas: insights from Mt Lamington, Papua New Guinea. Philos. Trans. R. Soc. A Math. Phys. Eng. Sci. 377: 20180018. https://doi.org/10.1098/rsta.2018.001.

Humphreys, M.C.S., Cooper, G.F., Zhang, J., Loewen, M., Kent, A.J.R., Macpherson, C.G., Davidson, J.P., 2019. Unravelling the complexity of magma plumbing at Mount St.

Helens: a new trace element partitioning scheme for amphibole. Contrib. Mineral. Petrol. 174, 9. https://doi.org/10.1007/s00410-018-1543-5.
Ishibashi, H., Suwa, Y., Miyoshi, M., Yasuda, A., Hokanishi, N., 2018. Amphibole–melt disequilibrium in silicic melt of the Aso-4 caldera-forming eruption at Aso Volcano, SW Japan. Earth, Planets and Space 70, 137. https://doi.org/10.1186/s40623-018-0907-4.
Jeffery, A.J., Gertisser, R., Troll, V.R., Jolis, E.M., Dahren, B., Harris, C., Tindle, A.G., Preece, K., O'Driscoll, B., Humaida, H., Chadwick, J.P., 2013. The pre-eruptive magma plumbing system of the 2007–2008 dome-forming eruption of Kelut volcano, East Java. Indonesia. Contrib. Mineral. Petrol. 166, 275–308.
Johnson, M.C., Rutherford, M.J., 1989. Experimental calibration of the aluminum-in-hornblende geobarometer with application to Long Valley caldera (California) volcanic rocks. Geology 17 (9), 837–841.
Kamac, O., Altunkaynak, Ş., 2019. Magma chamber processes and dynamics beneath northwestern Anatolia: Insights from mineral chemistry and crystal size distributions (CSDs) of the Kepsut volcanic complex (NW Turkey). J. Asian Earth Sciences 181, 103889.
Kiss, B., Harangi, S., Ntaflos, T., Mason, P.R., Pál-Molnár, E., 2014. Amphibole perspective to unravel pre-eruptive processes and conditions in volcanic plumbing systems beneath intermediate arc volcanoes: a case study from Ciomadul volcano (SE Carpathians). Contrib. Mineral. Petrol. 167 (3), 1–27.
Klaver, M, Matveev, S, Berndt, J., Lissenberg, C.J, Vroon, P.Z, 2017. A mineral and cumulate perspective to magma differentiation at Nisyros volcano, Aegean arc. Contrib. Mineral. Petrol. 172:95. https://doi.org/10.1007/s00410-017-1414-5.
Konečný, V., Kováč, M., Lexa, J., Šefara, J., 2002. Neogene evolution of the Carpatho–Pannonian region: an interplay of subduction and back-arc diapiric uprise in the mantle. EGS Special Publication Series 1, 165–194.
Kovacs, M., 2002. Petrogenesis of Subduction-Related Igneous Rocks from the Central-Southeastern Area of the Gutâi Mts Editura Dacia Cluj-Napoca. 201 pp. (in Romanian).
Kovacs, M., Fülöp, A., 2003. Neogene volcanism in the Gutâi Mts. (Eastern Carpathians): a review. Studia Universitatis Babeş-Bolyai, Geologia 48, 3–16.
Kovacs, M., Fülöp, A., 2005. Petrological and volcanological data of Piatra Rosie-Danesti extrusive domes in Gutai Mts., (Eastern Carpathians, România). Mineralia Slovaca 3 (37/2005), 285–287.
Kovacs, M., Fülöp, A., 2010. Laleaua Alba quarry: a Neogene composite igneous body. In: Iancu, O.G., Kovacs, M. (Eds.), Ore Deposits and Other Classic Localities in the Eastern Carpathians: From Metamorphics to Volcanics, IMA 2010 Field Trip Guide RO1. Acta Mineralogica-Petrographica vol. 19, pp. 32–35.
Kovacs, M., Pécskay, Z., Fülöp, A., Jurje, M., Edelstein, O., 2013. Geochronology of the Neogene intrusive magmatism of the Oaş-Gutâi Mts., Eastern Carpathians, NW Romania. Geol. Carpath. 64, 483–496.
Kovacs, M., Fülöp, A., Pécskay, Z., 2014. Dome-building volcanic activity in the Oaş-Gutâi Neogene Volcanic Area, Eastern Carpathians, Romania. Buletini i Shkencave Gjeologjike 1, 230–233.
Kovacs, M., Seghedi, I., Yamamoto, M., Fülöp, A., Pécskay, Z., Jurje, M., 2017. Miocene volcanism from the Oaş-Gutâi Volcanic Zone (Eastern Carpathians, Romania) – link to the geodynamic processes of Transcarpathian Basin. Lithos 294-295, 304–318.
Krawczynski, M.J., Grove, T.L., Behrens, H., 2012. Amphibole stability in primitive arc magmas: effects of temperature, H2O content, and oxygen fugacity. Contrib. Mineral. Petrol. 164 (2), 317–339.
Laeger, K., Halama, R., Hansteen, T., Savov, I.P., Murcia, H.F., Cortés, G.P., Garbe-Schönberg, D., 2013. Crystallization conditions and petrogenesis of the lava dome from the ~900 years BP eruption of Cerro Machín Volcano, Colombia. J. S. Am. Earth Sci. 48, 193–208.
Laumonier, M., Karakas, O., Bachmann, O., Gaillard, F., Lukács, R., Seghedi, I., Menand, T., Harangi, S., 2019. Evidence for a persistent magma reservoir with large melt content beneath an apparently extinct volcano. Earth Planet. Sci. Lett. 521, 79–90.
Leeman, W.P., Smith, D.R., 2018. The role of magma mixing, identification of mafic magma inputs, and structure of the underlying magmatic system at Mount St. Helens. Am. Mineral. 103, 1925–1944.
Lexa, J., Seghedi, I., Németh, K., Szakács, A., Konečný, V., Pécskay, Z., Fülöp, A., Kovacs, M., 2010. Neogene–Quaternary volcanic forms in the Carpathian–Pannonian Region: a review. Central European Journal of Geosciences 2 (3), 207–270.
Lindsley, D.H., 1983. Pyroxene thermometry. Am. Mineral. 68, 477–493.
Lindsley, D.H., Anderson, D.J., 1983. A two-pyroxene thermometer. J. Geophys. Res. 88, A887–A906.
Locock, A.J., 2014. An Excel spreadsheet to classify chemical analyses of amphiboles following the IMA 2012 recommendations. Comput. Geosci. 62, 1–11.
Lucci, F., Carrasco-Núñez, G., Rossetti, F., Theye, T., White, J.C., Urbani, S., Azizi, H., Asahara, Y., Giordano, G., 2020. Anatomy of the magmatic plumbing system of Los Humeros Caldera (Mexico): implications for geothermal systems. Solid Earth 11, 125–159.
Lukacs, R., Harangi, S., Guillong, M., Bachman, O., Fodor, L., Buret, Y., Dunk, I., Sliwinski, J., von Quad, A., Peytcheva, I., Zimmer, M., 2018. Early to Mid-Miocene syn-extensional massive silicic volcanism in the Pannonian Basin (East-Central Europe): Eruption chronology, correlation potential and geodynamic implications. Earth-Science Reviews 179, 1–19.
Martel, C., Pichavant, M., Holtz, F., Scaillet, B., Bourdier, J.-L., Traineau, H., 1999. Effects of fO2 and H2O on andesite phase relations between 2 and 4 kbar. J. Geophys. Res. Solid Earth 104 (B12), 29453–29470.
Martel, C., Andújar, J., Mothes, P., Scaillet, B., Pichavant, M., Molina, I., 2018. Storage conditions of the mafic and silicic magmas at Cotopaxi. Ecuador. J. Volcanol. Geotherm. Res. 354, 74–86.
Márton, E., Tischler, M., Csontos, L., Fügenschuh, B., Schmid, S.M., 2007. The contact zone between the ALCAPA and Tisza–Dacia mega-tectonic units of Northern Romania in the light of new paleomagnetic data. Swiss J. Geosci. 109, 109–124.
Molina, J.F., Moreno, J.A., Castro, A., Rodríguez, C., Fershtater, G.B., 2015. Calcic amphibole thermobarometry in metamorphic and igneous rocks: New calibrations based on plagioclase/amphibole Al-Si partitioning and amphibole/liquid Mg partitioning. Lithos 232, 286–305.
Morimoto, N., Fabries, J., Ferguson, A.K., Ginzburg, I.V., Ross, M., Seifert, F.A., Zussman, J., Aoki, K., Gottardi, G., 1988. Nomenclature of pyroxenes. Am. Mineral. 73, 1123–1133.
Murcia, H., Borrero, C., Németh, K., 2019. Overview and plumbing system implications of monogenetic volcanism in the northernmost Andes' volcanic province. J. Volcanol. Geotherm. Res. 383, 77–87.
Murray, K.E., Ducea, M., Schoenbohm, L., 2015. Foundering-driven lithospheric melting: the source of central Andean mafic lavas on the Puna Plateau (22°S–27°S). Geol. Soc. Am. Mem. 212, 139–166.
Mutch, E.J.F., Blundy, J.D., Tattitch, B.C., Cooper, F.J., Brooker, R.A., 2016. An experimental study of amphibole stability in low-pressure granitic magmas and a revised Al-inhornblende geobarometer. Contrib. Mineral. Petrol. 171, 1–27.
Nandedkar, R.H., Hürlimann, N., Ulmer, P., Müntener, O., 2016. Amphibole–melt trace element partitioning of fractionating calc-alkaline magmas in the lower crust: an experimental study. Contrib. Mineral. Petrol. 171 (8–9), 71. https://doi.org/10.1007/s00410-016-1278-0.
Naumov, V.B., Kovalenker, V.A., Damian, G., Abramov, S.S., Tolstykh, M.L., Prokofiev, V.Yu., Damian, F., Seghedi, I., 2014. Origin of the Laleaua Alba dacite (Baia Sprie volcanic area and Au-Pb-Zn ore district, Romania): evidence from study of melt inclusions. Central European Geology 57 (1), 83–112.
Neave, A.D., Putirka, K.D., 2017. A new clinopyroxene-liquid barometer, and implications for magma storage pressures under Icelandic rift zones. Am. Mineral., 102, 777–794.
Nimis, P., 1995. A clinopyroxene geobarometer for basaltic system based on crystal-structure modeling. Contrib. Mineral. Petrol. 121, 115–125.
Nimis, P., 1999. Clinopyroxene geobarometry of magmatic rocks. Part 2. Structural geobarometers for basic to acid, tholleitic and mildly alkaline systems. Contrib. Mineral. Petrol. 135, 62–74.
Nimis, P., Taylor, W.R., 2000. Single clinopyroxene thermobarometry for garnet peridotites. Part 1. Calibration and testing of a Cr-in-cpx barometer and an enstatite-in-cpx thermometer. Contrib. Mineral. Petrol. 139, 541–554.
Pécskay, Z., Lexa, J., Szakács, A., Kadosa, B., Seghedi, I., Konečny, V., Kovacs, M., Marton, E., Széky-Fux, V., Póka, T., Gyarmaty, P., Edelstein, O., Roşu, E., Žec, B., 1995. Space and time distribution of Neogene–Quaternary volcanism in the Carpatho–Pannonian Region. Acta Vulcanol. 7, 15–29.
Pécskay, Z., Lexa, J., Szakács, A., Seghedi, I., Balogh, K., Konečný, V., Zelenka, T., Kovacs, M., Póka, T., Fülöp, A., Márton, E., Panaiotu, C., Cvetković, V., 2006. Geochronology of Neogene–Quaternary magmatism in the Carpathian arc and Intra-Carpathian area: a review. Geol. Carpath. 57, 511–530.
Peters, S.T.M., Troll, V.R., Weis, F.A., Dallai, L., Chadwick, J.P., Schulz, B., 2017. Amphibole megacrysts as a probe into the deep plumbing system of Merapi volcano, Central Java. Indonesia. Contrib. Mineral. Petrol. 172, 16. https://doi.org/10.1007/s00410-017-1338-0.
Pichavant, M., Martel, C., Bourdier, J.-L., Scaillet, B., 2002. Physical conditions, structure, and dynamics of a zoned magma chamber: mount Pele'e (Martinique, Lesser Antilles Arc). J. Geophys. Res. 107 (B5), 1–28.
Pietranik, A., Holtz, F., Koepke, J., Puziewicz, J., 2009. Crystallization of quartz dioritic magmas at 2 and 1 kbar: experimental results. Mineral. Petrol. 97, 1–21.
Pouchou, J.L., Pichoir, F., 1991. Quantitative analysis of homogeneous or stratified microvolumes applying the model "PAP". In: Heinrich, K.F.J., Newbury, D.E. (Eds.), Electron Probe Quantitation. Plenum Publishing Corporation, New York, pp. 31–75.
Preece, K., Barclay, J., Gertisser, R., Herd, R.A., 2014. Textural and micro-petrological variations in the eruptive products of the 2006 dome-forming eruption of Merapi volcano, Indonesia: implications for sub-surface processes. J. Volcanol. Geotherm. Res. 261, 98–120.
Price, R.C., Gamble, J.A., Smith, I.E.M., Maas, R., Waight, T.E., Stewart, R.B., Woodhead, J., 2012. The anatomy of an andesitic volcano: a timestratigraphic study of andesite petrogenesis and crustal evolution at Ruapehu Volcano, New Zealand. J. Petrol. 53, 2139–2189.
Prouteau, G., Scaillet, B., 2003. Experimental constraints on the origin of the 1991 Pinatubo dacite. J. Petrol. 44, 2203–2241.
Putirka, K., 1999. Clinopyroxene-liquid equilibria to 100 kbar and 2450 K. Contrib. Mineral. Petrol. 135, 151–163.
Putirka, K., 2008. Thermometers and barometers for volcanic systems. Rev. Mineral. Geochem. 69, 61–120.
Putirka, K., 2016. Amphibole thermometers and barometers for igneous systems and some implications for eruption mechanisms of felsic magmas at arc volcanoes. Am. Mineral. 101 (4), 841–858.
Putirka, K., Johnson, M., Kinzler, R., Longhi, J., Walker, D., 1996. Thermobarometry of mafic igneous rocks based on clinopyroxene-liquid equilibria, 0–30 kbar. Contrib. Mineral. Petrol. 123, 92–108.
Putirka, K., Ryerson, F.J., Mikaelian, H., 2003. New igneous thermobarometers for mafic and evolved lava compositions, based on clinopyroxene-liquid equilibria. Am. Mineral. 88, 1542–1554.
Reed, S.B., 1990. Fluorescence effects in quantitative microprobe analysis. In: Williams, D.B., Ingram, P., Michael, J.R. (Eds.), Microbeam Analysis – 1990. San Francisco Press, San Francisco, pp. 109–114.
Ridolfi, F., Renzulli, A., 2012. Calcic amphiboles in calc-alkaline and alkaline magmas: thermobarometric and chemometric empirical equations valid up to 1130 °C and 2.2 GPa. Contrib. Mineral. Petrol. 163, 877–895.
Ridolfi, F., Renzulli, A., Puerini, M., 2010. Stability and chemical equilibrium of amphibole in calc-alkaline magmas: an overview, new thermobarometric formulations and application to subduction related volcanoes. Contrib. Mineral. Petrol. 160, 45–66.
Rutherford, J.M., Devine, J.D., 2003. Magmatic conditions and magma ascent as indicated by hornblende phase equilibria and reactions in the 1995-2002 Soufriere Hills Magma. J. Petrol. 44(8), 1433–1453.

Săndulescu, M., Visarion, M., Stănică, D., Stănică, M., Atanasiu, L., 1993. Deep structure of the inner carpathians in the maramureş-tisa zone (East Carpathians). Rom. J. Geophysics 16, 67–76.
Sato, H., Holtz, F., Botcharnikov, R.E., Nakada, S., 2017. Intermittent generation of mafic enclaves in the 1991-1995 dacite of Unzen Volcano recorded in mineral chemistry. Contrib. Mineral. Petrol. 172:22. https://doi.org/10.1007/s00410-017-1335-3.
Sato, H., Holtz, F., Behrens, H., Botcharnikov, R., Nakada, S., 2005. Experimental petrology of the 1991–1995 Unzen dacite, Japan. Part II: cl/OH partitioning between hornblende and melt and its implications for the origin of oscillatory zoning of hornblende phenocrysts. J. Petrol. 46 (2), 339–354.
Scaillet, B., Evans, B.W., 1999. The 15 June 1991 eruption of mount pinatubo. I. phase equilibria and pre-eruption P–T–fO2–fH2O conditions of the dacite magma. J. Petrol. 40 (3), 381–411.
Schmid, S.M., Bernoulli, D., Fügenschuh, B., Matenco, L., Schefer, S., Schuster, R., Tischler, M., Ustaszewski, K., 2008. The Alpine-Carpathian-Dinaridic orogenic system: correlation and evolution of tectonic units. Swiss J. Geosci. 101, 139–183.
Schmidt, M.W., 1992. Amphibole composition in tonalite as a function of pressure: an experimental calibration of the Al-in-hornblende barometer. Contrib. Mineral. Petrol. 110 (2–3), 304–310.
Seghedi, I., Downes, H., 2011. Geochemistry and tectonic development of Cenozoic magmatism in the Carpathian–Pannonian region. Gondwana Res. 20, 655–672.
Seghedi, I., Downes, H., Pécskay, Z., Thirlwall, M.F., Szakács, A., Prychodko, M., Mattey, D., 2001. Magmagenesis in a subduction-related post-collisional volcanic arc segment: the Ukrainian Carpathians. Lithos 57, 237–262.
Seghedi, I., Downes, H., Szakács, A., Mason, T.R.D., Thirlwall, M.F., Rosu, E., Pécskay, Z., Márton, E., Panaiotu, C., 2004. Neogene–Quaternary magmatism and geodynamics in the Carpathian–Pannonian region: a synthesis. Lithos 72, 117–146.
Shane, P., Smith, V.C., 2013. Using amphibole crystals to reconstruct magma storage temperatures and pressures for the post-caldera collapse volcanism at Okataina volcano. Lithos 156–159, 159–170.
Sisson, T.W., Grove, T.L., 1993. Experimental investigations of the role of H2O in calc-alkaline differentiation and subduction zone magmatism. Contrib. Mineral. Petrol. 113, 143–166.
Sparks, R.S.J., Annen, C., Blundy, J.D., Cashman, K.V., Rust, A.C., Jackson, M.D., 2019. Formation and dynamics of magma reservoirs. Philos. Trans. R. Soc. A. https://doi.org/10.1098/rsta.2018.0019.
Springer, G., 1971. Fluorescence by the X-ray continuum in multi-element targets: Falconbridge Nickel Mines Limited. Thornhill, Ontario, Canada, Report FRL-138 14 p.
Szakács, A., Pécskay, Z., Silye, L., Balogh, K., Vlad, D., Fülöp, A., 2012. On the age of the Dej Tuff, Transylvanian Basin, Romania. Geol. Carpath. 63, 138–148.
Szepesi, J., Lukács, R., Soós, I., Benkó, Z., Pécskay, Z., Ésik, Z., Kozák, M., Di Capua, A., Groppelli, G., Norini, G., Sulpizio, S., Sz, Harangi, 2019. Telkibánya lava domes: Lithofacies architecture of a Miocene rhyolite field (Tokaj Mountains, Carpathian-Pannonian region, Hungary). J. Volcanol. Geotherm. Res. https://doi.org/10.1016/j.jvolgeores.2019.07.002.
Tischler, M., Gröger, H.R., Fügenschuh, B., Schmid, S.M., 2007. Miocene tectonics of the Maramures area (northern Romania): implications for the mid-Hungarian fault zone. Int. J. Earth Sci. 96, 473–496.
Tischler, M., Mațenco, L., Filipescu, S., Gröger, H.R., Wetzel, A., Fügenschuh, B., 2008. Tectonics and sedimentation during convergence of the ALCAPA and Tisza-Dacia continental blocks: The Pienide nappe emplacement and its foredeep (N. Romania). In: Siegesmund, S., Fügenschuch, B., Froitzheim, N. (Eds.), Tectonic Aspects of the Alpine-Dinaride-Carpathian System. Geological Society of London Special Publications vol. 298, pp. 317–334.
Turner, S.J., Izbekov, P., Langmuir, C., 2013. The magma plumbing system of Bezymianny Volcano: insights from a 54 year time series of trace element whole-rock geochemistry and amphibole compositions. J. Volcanol. Geotherm. Res. 263, 108–121.
Ubide, T., Kamber, B.S., 2018. Volcanic crystals as time capsules of eruption history. Nat. Commun. 9, 326. https://doi.org/10.1038/s41467-017-02274-w.
Ulmer, P., Kaegi, R., Muntener, O., 2018. Experimentally derived intermediate to silica-rich arc magmas by fractional and equilibrium crystallization at 1.0 GPa: an evaluation of phase relationships, compositions, liquid lines of descent and oxygen fugacity. J. Petrol. 59 (1), 11–58. https://doi.org/10.1093/petrology/egy017.
Wanke, M., Karakas, O., Bachmann, O., 2019. The genesis of arc dacites: the case of Mount St. Helens, WA. Contrib. Mineral. Petrol. 74, 7. https://doi.org/10.1007/s00410-018-1542-6.
Wells, P.R.A., 1977. Pyroxene thermometry in simple and complex systems. Contrib. Mineral. Petrol. 62, 129–139.
Wood, B.J., Banno, S., 1973. Garnet-Orthopyroxene and Orthopyroxene-Clinopyroxene relationships in simple and complex systems. Contrib. Mineral. Petrol. 42, 109–124.